

## UvA-DARE (Digital Academic Repository)

### Pseudorotaxane strategies for guiding self-assembly and the application of molecular machinery in photoelectrochemical devices

Bouwens, T.

**Publication date**  
2021

[Link to publication](#)

#### **Citation for published version (APA):**

Bouwens, T. (2021). *Pseudorotaxane strategies for guiding self-assembly and the application of molecular machinery in photoelectrochemical devices*.

#### **General rights**

It is not permitted to download or to forward/distribute the text or part of it without the consent of the author(s) and/or copyright holder(s), other than for strictly personal, individual use, unless the work is under an open content license (like Creative Commons).

#### **Disclaimer/Complaints regulations**

If you believe that digital publication of certain material infringes any of your rights or (privacy) interests, please let the Library know, stating your reasons. In case of a legitimate complaint, the Library will make the material inaccessible and/or remove it from the website. Please Ask the Library: <https://uba.uva.nl/en/contact>, or a letter to: Library of the University of Amsterdam, Secretariat, Singel 425, 1012 WP Amsterdam, The Netherlands. You will be contacted as soon as possible.

# Chapter 4

## Supramolecular Organization in Artificial Photosynthesis

*Part of this work has been published as:*

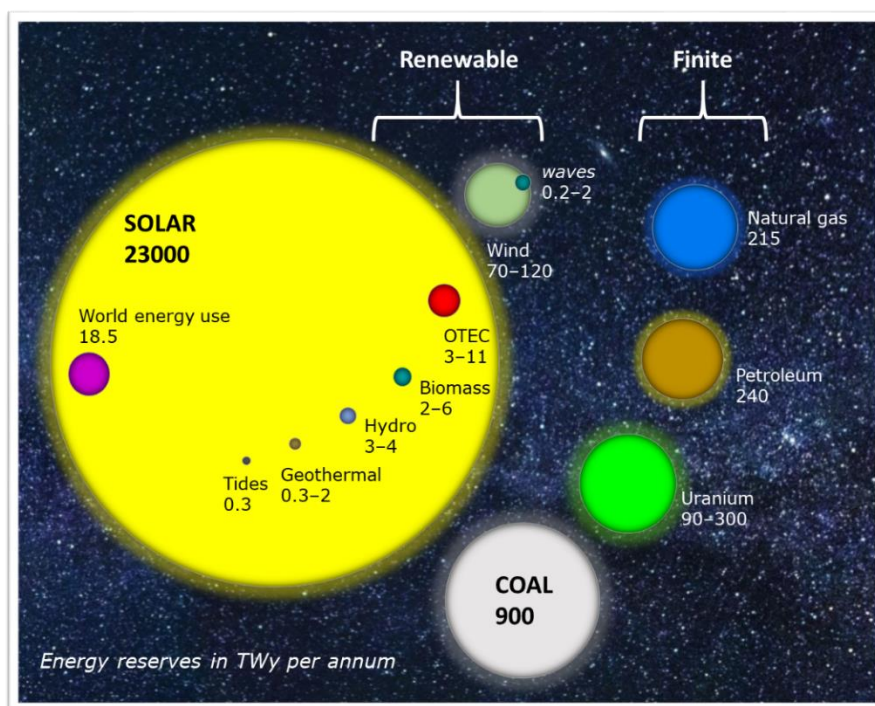
Tom Keijer, Tessel Bouwens, Joeri Hessels and Joost N. H. Reek, *Supramolecular strategies in artificial Photosynthesis, Chem. Sci.*, **2021**, *12*, 50–70.

## 1. Towards sustainable energy sources

Burning fossil fuels has catastrophic effects on our climate and demands for a new sustainable energy supply. The yearly energy consumption in 2019 was 19.8 TWy (terawatt–year), and this is estimated to increase to 27 TWy in 2050.<sup>[1,2]</sup> Nowadays, approximately 80% (16 TW) of this energy originates from greenhouse gas emitting sources causing global warming.<sup>[2,3]</sup> To counteract the high CO<sub>2</sub> emission originating from burning of fossil fuels, a drastic transition to renewable energy sources is essential. The term “renewable” implies that these energy sources are restored within one (human) generation, such as wind energy, hydro power, thermal energy, biomass and solar power. Figure 1 shows an estimation of the renewable and finite energy reserves. The total recoverable reserves for the finite resources are slowly being depleted while the yearly potential for sustainable sources are renewed within a yearly cycle. The *International Energy Agency Solar Heating and Cooling Programme* reviewed that a sustainable energy mix of these renewable energy sources is the best approach to transition to a sustainable society “akin to putting future energy eggs in different baskets” as was stated by Perez *et al.*<sup>[1]</sup> Comparing all the sustainable alternatives in Figure 1, the only source that can meet our current and future yearly energy demand is the sun.<sup>[4]</sup> This demand is simply 0.1% of the energy that is delivered by the sun every year, hence harnessing merely a fraction of solar potential already suffices to meet the world’s entire energy demand.<sup>[1,5]</sup> Therefore, *International Energy Agency Solar Heating and Cooling Programme* state that the focus of sustainable energy resources of the future should be on solar technologies.

One major challenge for a sustainable energy supply is that most of the renewable energy sources are intermittent as, for example, there is no sunlight at night providing an irregular power supply. Next to that, a household’s electricity consumption is greatest at night used for cooking, heating and illuminating. To solve this challenge, the energy that is obtained should be stored, for example in batteries or fuels. Currently, 80% of our energy consumption is fuel based and therefore shifting to green energy carriers generated with sunlight is vital to transition to a sustainable society.<sup>[2,3]</sup> To approach this, scientists are inspired by nature that has been employing the photosynthetic process for millions of years that uses solar light energy to convert water and CO<sub>2</sub> into the building blocks of life. The field of artificial photosynthesis strives to harness solar energy as chemical potential to ultimately create sustainable fuels, such as H<sub>2</sub>. The photosynthetic process requires three main actions: 1) **light harvesting**, 2) **charge-separation** and 3) **catalysis**. As these fundamental actions take place on such different timescales varying from picoseconds to seconds, integrating all actions into one device is extremely complicated and demands an interdisciplinary approach. To design artificial photosynthetic devices there are two different strategies employed: 1) a direct

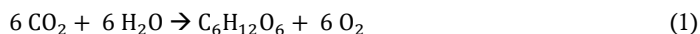
approach, where solar power is directly converted into electricity or a fuel or, 2) an indirect approach, where solar energy is first converted into electric potential that can drive fuel generation in a device, e.g., a solar cell that powers a water electrolyzer to produce H<sub>2</sub> from water splitting. These two types of solar-to-fuel devices use natural photosynthesis as a blueprint, inspired by the light harvesting complexes and enzymes that catalyze the light-to-chemical transformations in plants, cyanobacteria and algae. Looking closer, the photosynthetic apparatus can be found within the thylakoid membrane within these organisms, where all the components for light harvesting and catalysis are well-organized within a protein matrix to facilitate efficient (proton-coupled) electron transfer steps.<sup>[6]</sup> Supramolecular interactions play a major role within the protein environment to retain this crucial organization of (photo)electronically active motifs at specific orientations and distances. Therefore, using supramolecular organization in artificial photosynthesis could be a great strategy to promote the three fundamental actions required in the solar-to-fuel conversion process. The following part discusses photosynthesis and the current role of supramolecular chemistry in devices for solar conversion applications.



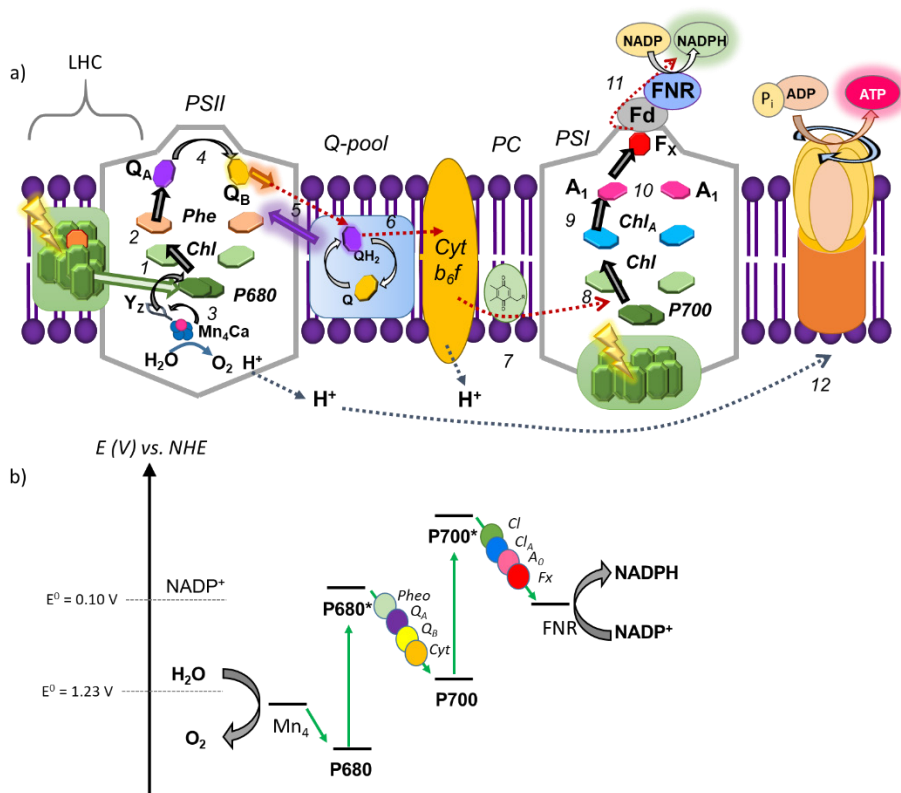
**Figure 1.** Estimated finite and renewable planetary energy reserves in 2015 (Terawatt-years) together with the world energy use in 2019. The yearly potential is shown for the renewables and the total recoverable reserves are shown for the finite resources for 2015.<sup>[1]</sup> OTEC = Ocean Thermal Energy Conversion.

## 2 Fundamental actions in photosynthesis

Oxygenic photosynthesis is a photochemical process that uses solar energy for the synthesis of carbohydrates and dioxygen from CO<sub>2</sub> and H<sub>2</sub>O (Equation 1).



These carbohydrates are the basis of our food supply and therefore, photosynthesis is a fundamental process that provides the energy for the survival of humankind. Photosynthesis involves a collection of extremely complex photophysical and photochemical transformations taking place within the chloroplast organelle of the plant cell. The chloroplast consists of thylakoids, cavities wrapped in bilayer membrane, where the light harvesting complexes (LHC) are embedded together with photosystems I and II (PSI, PSII) (Figure 2). The photosystems absorb photons to induce energy and electron transfer steps (Figure 2b).<sup>[7-9]</sup>



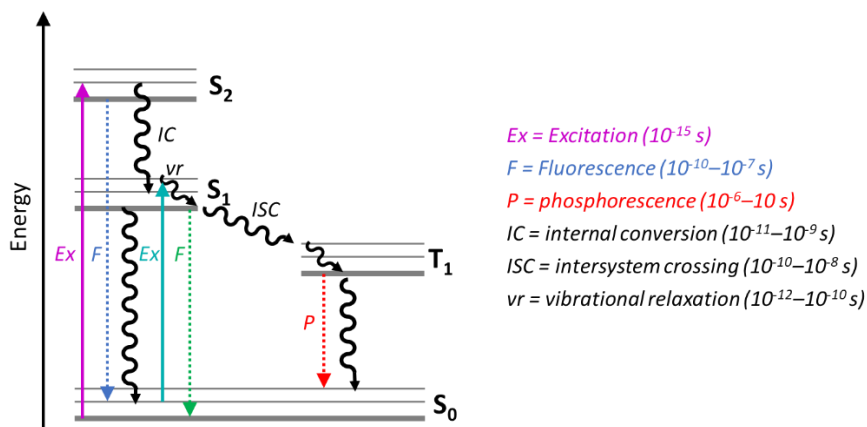
**Figure 2.** a) Schematic representation of the thylakoid membrane in plants with the four major complexes that participate in the light reactions. b) Z-scheme of photosynthetic reactions. Double excitation is used to drive the uphill reaction to harness electrons from water splitting in NADP<sup>+</sup> to form NADPH. This figure is inspired on schemes from Stryer *et al.*<sup>[10]</sup>

## 2.1. The photophysics of light harvesting

Light harvesting is the first fundamental action in photosynthesis. The absorption of photons is required to induce a transition of an electron from the ground state to a higher electronic state creating an excited state, coinciding with a redistribution of electron density in the light absorbing molecule. Box 1 and Figure 3 summarize the principles of electronic excitations in a Jablonski diagram.

### Box 1. Electronic excitations

The excitation of an electron is described with frontier orbital theory, which is explained as light absorption leading to an excitation from the highest occupied molecular orbital (HOMO) to the lowest unoccupied orbital (LUMO).<sup>[11]</sup> The corresponding energy gap often translates into the color we observe for that pigment.<sup>[10,12]</sup> Upon excitation, the molecule relaxes to lower vibrational states through internal conversion via intra-molecular vibrations and inter-molecular collisions with solvent molecules. Other decay pathways include fluorescence and inter-system crossing (ISC) to yield a triplet state, from where phosphorescence can take place. Fluorescence and phosphorescence are radiative decay pathways where light emission is allowed to take place. A lower energy photon is emitted from the lowest excited state of a given multiplicity (Kasha's rule). The molecule can also relax back to the ground state via non-radiative decay via release of heat instead of photons.



**Figure 3.** Jablonski diagram with energy levels representing the electronic transitions and associated decay pathways of pigments along with the time scales at which these events take place. The ground state ( $S_0$ ) can be regarded as the HOMO while the LUMO is considered as the first electronic excited state ( $S_1$ ). Excitation can also lead to the second excited state ( $S_2$ ) or formation of a triplet state ( $T_1$ ). Decay pathways can be either radiative (colored dashed lines) or non-radiative (black wavy lines). Ex = excitation F = Fluorescence IC = internal conversion, vr = vibrational relaxation, ISC = intersystem crossing, P = phosphorescence.

Nature employs highly-ordered supramolecular architectures, dedicated to light capture and energy transmittance, to funnel energy from harvested light to the reaction center via an energy cascade (Figure 2, Step 1).<sup>[13]</sup> For optimal light absorption of all colors the light harvesting complex comprises of many alternative colored pigments. These pigments are carotenoids (Figure 2, orange) and chlorophylls (Figure 2, green) e.g. porphyrinoids substituted with a plethora of residues to achieve a high range of photon absorption.<sup>[14]</sup> All components in both LHCs are organized in a certain way via supramolecular interactions inducing a specific orientation, such as *J*-aggregates.<sup>[15,16]</sup> This orientation engenders enhanced delocalization of excitons (electron–hole pair) across several of the same chromophores for rapid energy transfer amongst them. The light harvesting complex is therefore also called the antenna complex. The close packing of pigments within the antenna complex does not lead to quenching of the delocalized exciton as new electronic properties emerge from this *J*-mode that prevent this. Rapid energy transfer enables transport of concentrated photon energy to the reaction center. The reaction center itself also has a specific spatial orientation from which unique photophysical properties emerge, made possible through supramolecular interactions. The energy cascade transfers photonic energy via multiple electronic energy transfer (EET) steps to the reaction center at the expense of small energy losses. Concurrently, back transfer of the propagated electron is prevented, as this is energetically uphill, inducing directionality into the transfer steps to enable charge separation within the reaction center.

## 2.2. Charge separation in Nature: electron transfer and Marcus theory

After photonic energy transfer to the reaction center, photoinduced electron transfer is promoted in the photosynthetic apparatus. The underlying principles of electron transfer are described in Box 2. The funneled photon energy is used for charge separation in the reaction center through further electron transfer from *P680* to *Pheo* to form *P680<sup>+</sup>Pheo<sup>•</sup>* (Figure 2, Step 1).<sup>[17]</sup> The positive charge on this pigment is neutralized by an electron extracted from water splitting (Figure 2, Step 3). This initiates the linear electron transfer pathway (Figure 2, Step 4) to a permanently bound quinone molecule *Q<sub>A</sub>* that then reduces exchangeable quinone molecule (*Q<sub>B</sub>*) to hydroquinone (*QH<sub>2</sub>*).<sup>[17]</sup> Quinones are held in place within the binding pocket via hydrogen bonds (H-bonds). Upon reduction of *Q<sub>B</sub>* the H-bonds are broken and *QH<sub>2</sub>* moves away to the quinone pool, making room for a new *Q<sub>A</sub>* (Figure 2, Step 5) molecule.<sup>[18–20]</sup> The cytochrome *bf* complex (*cyt b<sub>6</sub>f*) uses *QH<sub>2</sub>* to reduce plastocyanin (PC) (Figure 2, Step 6–7) that functions as the electron donor in PSI (Figure 2, Step 8). PSI is excited through absorption of another photon to facilitate transfer (Figure 2, Step 9–10) of the high energy electron, which is ultimately used for the reduction of nicotinamide adenine dinucleotide phosphate (NADP<sup>+</sup>) to NADPH (Figure 2, Step 11). NADPH is the terminal

electron carrier used for further redox chemistry in the cell such as the fixation of carbon dioxide to ultimately create carbohydrates.

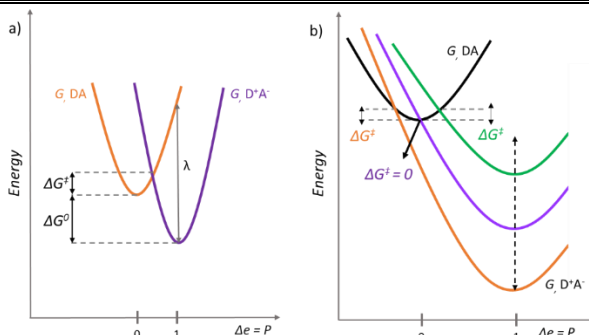
### *2.3 Efficient charge separation follows the uphill catalytic formation of NADPH<sup>+</sup>*

In the event that an electron has been transferred and the  $D^+A^-$  pair has formed, a charge separated state is created. After photoinduced electron transfer (PET), charge recombination of  $D^+A^-$  back to  $D-A$  results in the dissipation of the absorbed photon energy. In PSII of the photosynthetic apparatus, recombination is inhibited by fast quenching of the  $P680^+$  pigment and by removal of the exchangeable  $Q_H$  for  $Q_B$ . The sequential electron transfer pathway in PSII ensures that slow water oxidation (ms timescale) and fast ET (ps timescale) can take place in parallel, while recombination becomes less likely with every step by removing  $A^-$  further away in space from  $D^+$ .

In PSI, unproductive charge recombination is believed to be inhibited as this ET reaction takes place in the Marcus inverted region.<sup>[21]</sup> PET in natural photosynthesis makes optimal use of photonic energy, demonstrating a remarkably high quantum efficiency, while charge recombination has been suppressed to a minimum.<sup>[12]</sup> In summary, Nature drives the endergonic (uphill) reaction from catalytic splitting of water to reduce  $NADP^+$  to NADPH with photonic energy (Figure 2b). This (terminal) electron carrier is used to drive subsequent reduction reactions, such as carbon fixation to ultimately create glucose from  $CO_2$ .



## Box 2. Dynamics of electron transfer: Marcus Theory



**Figure 4.** Schematic diagram for the parabolic outer sphere reorganization energies for a general D–A ET system. a) The parabolas represent the solvent polarization conditions ( $P$ ) for G, DA before ET (orange) and after ET (purple) for G, D<sup>+</sup>A<sup>-</sup>.  $\Delta G^\ddagger$  = activation energy;  $\Delta G^0$  = free energy driving force;  $\lambda$  = reorganization energy. b) G, DA before ET (black) and after ET with different thermodynamic driving force  $\Delta G^0$ .

Marcus theory describes the driving force ( $\Delta G^0$ ) of outer sphere electron transfer and the stability of the charge separated state afterwards. The theory is based on transition state theory (TST), but unlike chemical reaction mechanisms, electron transfer reactions are quantized. This implies that the electron is either fully located on D or A unlike a classical  $S_N2$  reaction. The direct atomic environment plays a key role in ET. The Franck-Condon Principle states that ET is fast in comparison to movement of the nuclei of atoms, i.e. the atomic orientations within D, A and surrounding solvent molecules remain unaffected. The consequent reorientation of the direct atomic environment, i.e. the solvent molecules requires energy, which is the activation barrier  $\Delta G^\ddagger$  of the ET reaction (Figure 4a). The two parabolic energies are described along the solvent polarization ( $P$  or  $\Delta e$ ) and the intersection is  $\Delta G^\ddagger$ . Most remarkable is that maximizing  $\Delta G^0$  does not necessarily lead to a higher driving force for ET reactions. Figure 4b shows three overlapping parabolas for ET with different reorganization energies. Going from the green to the purple parabola,  $\Delta G^\ddagger$  decreases to approximate  $\Delta G^\ddagger = 0$ , which is barrierless. However, moving onto the red parabola, although  $\Delta G^0$  is much lower,  $\Delta G^\ddagger$  is higher. This means that there is a lower thermodynamic driving force described as the Marcus inverted region.

The rate of an ET process is described as TST at a fixed distance, represented by equation 2.

$$k_{ET} = \sqrt{\frac{4\pi^3}{h^2 \lambda k_B T}} H_{AB}^2 \exp\left\{-\frac{(\Delta G + \lambda)^2}{4\lambda k_B T}\right\} \quad (2)$$

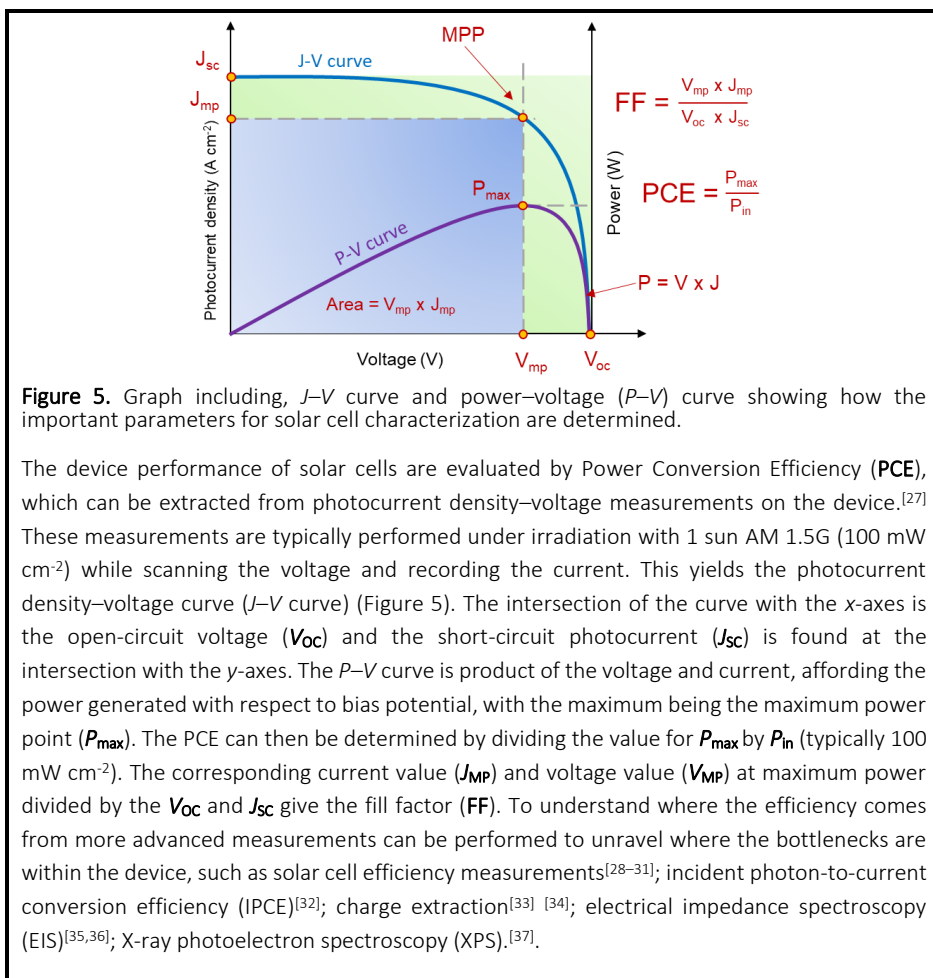
In this equation  $k_{ET}$  depends on the driving force for ET ( $\Delta G^0$ ), the reorganization energy  $\lambda$  and the electronic coupling between A and B  $H_{AB}$  where  $k_B$  is the Boltzmann constant,  $h$  is the Planck constant and  $T$  is temperature. The coupling constant  $H_{AB}$  and the rate of ET depend exponentially on the distance between D and A ( $d_{AB}$ , Equation 3).<sup>[25]</sup> The decay constant  $\beta$  is characteristic for the D–A pair. This implies that longer distances between D and A translate into a slower electron transfer rate.<sup>[26]</sup>

$$k_{ET} \propto \exp(-\beta d_{AB}) \quad (3)$$

### 3. Mimicking photosynthesis: From action to device

Natural photosynthesis carries out the three main actions (light harvesting, charge-separation and catalysis) within the thylakoid membrane of the chloroplast. With artificial photosynthetic devices, there is a distinction between devices integrating all three actions and technologies that couple two devices for respective solar power conversion and catalysis. Direct technologies for harnessing sun light include photovoltaics (PV) and solar-fuel generation in photoelectrochemical or photobiological cells. To determine efficiencies of solar cells, these devices are characterized using photocurrent density–voltage ( $J$ - $V$ ) curves, which is further discussed in Box 3.

#### Box 3. Device characterization of solar cell performance



The power generated in the PV cell can be used to drive an electrolyzer and thereby oxidize water and making oxygen (equation 4).<sup>[38,39]</sup>



The protons and electrons that are generated can be used to reduce CO<sub>2</sub> to hydrocarbons or create hydrogen as green fuel. The next part discusses these different solar conversion technologies.

### 3.1. PV-electrocatalysis

PV-electrocatalysis is an indirect method that uses the electric potential obtained from solar light to drive an electrolyzer that splits water. In principle, all PV methods (Si, perovskite, DSSC OPV) can be coupled to an electrolyzer. The most common PV method on the market is the single-junction silicon solar cell.<sup>[40]</sup> Relatively thick layers of highly pure silicon are required for efficient light harvesting in these type of p–n junctions imposing the production on high costs. Alternatively, state of the art perovskite solar cells are very promising exceeding 25% efficiency. The protocols for preparing these hybrid halides for PV has been improved tremendously since their discovery by Miyasaka.<sup>[41]</sup> However, the field struggles with efficient synthesis, long-term device stability and high toxicity of Pb<sup>2+</sup>—an essential element for efficient Perovskites—hampering general application.<sup>[42–45]</sup> For molecular approaches in PV, high purity of materials is less of an issue lowering the (theoretical) production costs. These solar cells use molecular components to convert solar power into electricity such as the dye-sensitized solar cell (DSSC) and organic photovoltaic cells (OPV). However, up to date inorganic p–n PV cells coupled to drive water splitting have reached the highest efficiency. The solar-to-hydrogen efficiency (STH) by coupling a Si solar cell to an electrolyzer is moderate (10–15%)<sup>[46]</sup>, but current optimization improved this technology significantly up to 30%.<sup>[47]</sup> Coupling a PV cell to drive water splitting with an electrolyzer is the most feasible strategy to generate solar-fuels in comparison to other solar technologies. Although production costs are high and the required materials are scarce, this strategy holds the current STH record.<sup>[48]</sup>

### 3.2. Single-compartment photoelectrochemical cells

Nocera's artificial leaf is an example of a wireless single compartment device, where light energy is used to split water into oxygen and hydrogen.<sup>[49]</sup> Fujishima and Honda showed that TiO<sub>2</sub> is able to oxidize water by absorbing solar light, which lead to the development of more semiconductors functionalized with catalyst for water splitting.<sup>[50,51]</sup> The big disadvantage of this strategy is that O<sub>2</sub> and H<sub>2</sub> are produced simultaneously, imposing some serious risks. A

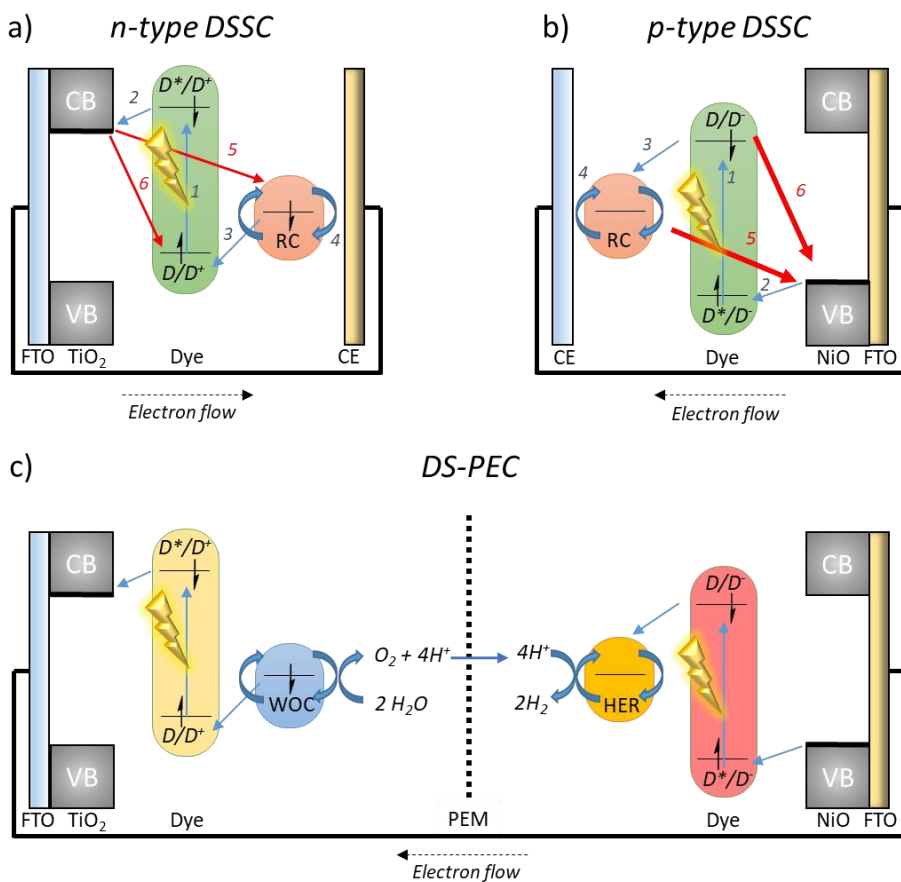
gas separating membrane is essential to include into the device before the produced hydrogen gas can be used.

### *3.3 Molecular solar cells and photoelectrochemical cells*

Two main technologies can be distinguished in the molecular based solar cell field: DSSCs and heterojunction based cells (OPV). Despite the difference in their operational principle, the challenges are similar to each other and also similar to natural systems, as light capturing, charge separation and charge carrier transport are the main contributors to the cell performance.

#### *3.3.1. Organic Photovoltaics (OPV)*

OPV cells consist of an organic semiconductor that, dependent of the size of the band gap, converts low energy IR or high energy UV light into electricity. The light absorbing material can consist of polymers or single molecules that both feature large conjugated systems. Upon photon absorption in the donor region, the delocalized  $\pi$ -electrons are excited creating an exciton.<sup>[52]</sup> This exciton consists of an electron–hole pair that is separated by an effective electric field, in this case, caused by the heterojunction. The electron is transferred from the donor to the acceptor at the heterojunction, breaking the exciton. The separated electron and hole (charge carriers) migrate to the contacts. Typically, donors and acceptors in OPV consist of conjugated molecules or polymers with large  $\pi$ -systems. An important requirement of the material is that charge carrier mobility must be sufficient in proportion to the thickness of the organic D–A layer, such that electrons and holes can reach the contacts of the cell. If the mobility is too low, the system is prone to charge recombination. This is often the case for planar heterojunctions. In this simple OPV type the organic material (acceptor-or-donor-type) is sandwiched between two contacts. To compensate for the typical diffusion length of the charge carriers (10 nm), the films have to be ultra-thin (<100 nm).<sup>[53]</sup> As a consequence, light absorption is low.<sup>[54]</sup> This is dealt by using bulk-heterojunction (BHJ) cell architectures. The donor (D) and acceptor (A) materials mixture has a phase separation of a few nanometers increasing the interfacial area for charge separation. This separation is essential and therefore control over morphology is the key aspect for efficient charge separation at the D–A interface. Control over molecular organization is therefore an important approach to achieve charge separation to obtain high efficiencies.<sup>[55]</sup> Current OPV cells have PCEs close to 17% making this a very promising technology.<sup>[56,57]</sup>



**Figure 6.** Schematic representation of operational mode of the DSSC (top) and the DS-PEC (bottom). In DSSCs the light absorbing dye molecule is anchored to a semiconductor that is applied onto a conducting substrate (Typically FTO glass). The dye performs charge-separation and oxidizes or reduces the redox couple (RC) in the electrolyte that delivers the charge to the counter electrode (CE) closing the circuit. a) For *n*-type the dye is excited (Process 1) followed by fast electron injection into the conduction band (CB) (Process 2). The dye is oxidatively quenched by the redox couple (Process 3). The redox couple is then regenerated at the counter electrode (CE) (Process 4). b) In *p*-type the electrons move the other way around, but the processes are equivalent to *n*-type. The dye is excited (Process 1) after which it is reductively quenched by an electron in the valence band (VB) of the NiO (Process 2). The electron of the reduced dye is transferred to the RC (Process 3) after which the redox mediator is regenerated at the CE (Process 4). The possible recombination pathways that compete with forward electron propagation (blue arrows) are depicted with red arrows. c) A DS-PEC performs processes light capturing and charge separation in a similar fashion. However, the RC is substituted for a redox catalyst performing reactions such as water splitting. The catalyst may be anchored to the semiconductor surface or dye as diffusion is not required. Water oxidation catalysts (WOC) oxidize water to oxygen and protons. Four oxidations are required to generate a single oxygen molecule. The hydrogen evolution catalyst (HEC) combines the electrons and protons liberated at the anode to form hydrogen gas at the cathode. Every hydrogen molecule requires two electrons from the HEC. The half reactions are often separated by a proton exchange membrane (PEM).

### 3.3.2. Dye-sensitized solar cells (DSSCs)

Dye-sensitized solar cells (DSSCs) are devices based on molecular components invented by Grätzel and O'Regan.<sup>[58]</sup> DSSCs parallel silicon based technologies, additionally benefiting from great performance under diffuse light conditions due to their mode of operation, which utilizes a photoinduced electron transfer, like photosynthesis. Furthermore, the large variety of color (from dyes) and shape possible (screen printing) allows for design opportunities, such as flexible cells or transparent solar cells for building integrating photovoltaics (BIPV).<sup>[59,60]</sup> The major difference with inorganic p-n junction based PV is that, in DSSC, light harvesting and charge separation are performed by different components. Therefore, the purity of material is less of an issue for DSSC and manufacturing does not require a clean room, reducing (theoretical) fabrication costs.<sup>[58]</sup> The operational principle of both *n*-type DSSCs and *p*-type DSSCs is represented in Figure 6a-b. Both configurations use a molecular dye for light absorption in an analogous fashion to pigments found in Nature's LHCs. This dye is attached to the semiconductor typically TiO<sub>2</sub> (for *n*-type) or NiO (for *p*-type), that is sintered onto a conducting substrate, such as fluorine doped tin oxide (FTO). Upon excitation of the dye (Figure 6, Process 1), injection of an electron (Figure 6, Process 2) into the conduction band (CB) for *n*-type occurs, or hole injection into the valence band (VB) for the complementary *p*-type DSSC. Regeneration of the dye is achieved by the redox mediator (Figure 6, Process 3). The redox couple diffuses between the working and counter electrodes, generating a current flow (Figure 6, Process 4). Forward electron propagation (Figure 6, blue arrows) competes with recombination pathways represented by red arrows (Figure 6, Process 5, 6) hampering the overall power conversion efficiency (PCE). While the TiO<sub>2</sub>-based *n*-type DSSCs exhibit PCE up to 14.3%,<sup>[59]</sup> PCEs are more lower in NiO-based *p*-type DSSC (current PCE record 2.51%).<sup>[61]</sup> The difference in PCE between *n*- and *p*-type DSSCs is attributed to the charge carrier characteristics of the semiconductor, as hole transport in NiO is significantly slow compared to the faster electron diffusion in TiO<sub>2</sub>, causing the former to experience greater amounts of charge recombination at the semiconductor–electrolyte interface (Figure 6b, Process 6) (see Section 3.7 for an elaborate explanation).<sup>[62–65]</sup> The poor performance of *p*-type DSSCs hampers the development of tandem photovoltaics and artificial photosynthetic devices for light-driven redox chemistry, such as dye-sensitized photoelectrochemical cells (DS-PECs) (see below Section 3.6). Therefore, this recombination issue in *p*-DSSCs must be addressed.<sup>[66,67]</sup>

### 3.3.3. Dye-sensitized photoelectrochemical cell (DS-PEC)

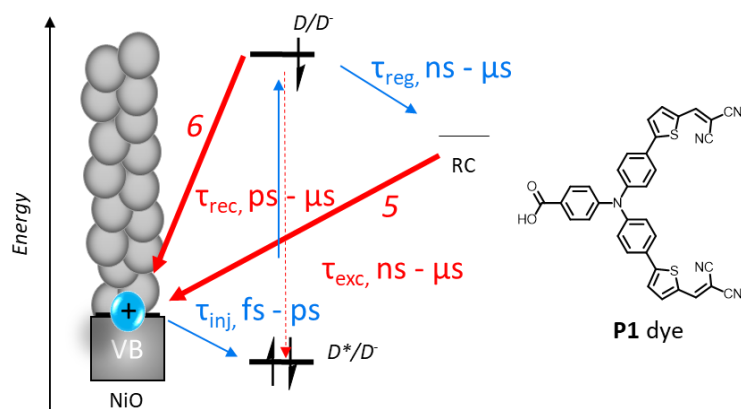
DS-PEC is closely related to DSSC, yet, the potential that is created upon dye excitation and injection is used to drive photoelectrochemical processes. Unlike a DSSC, which uses a redox mediator to close the circuit, a DS-PEC generates redox equivalents at the dye–electrolyte interface to drive electrocatalytic redox conversions including proton reduction to H<sub>2</sub>, CO<sub>2</sub> reduction, water oxidation, and alcohol oxidation.<sup>[68–72]</sup> Ultimately, the DS-PEC device design should include two compartments to generate electrons and protons via water splitting at the anode, instigating catalytic reduction reactions at the cathode. The most common solar-fuel generating-reaction is the reduction of protons (that are extracted from water oxidation) to H<sub>2</sub>, but these electrons and protons can also be used to reduce CO<sub>2</sub>.<sup>[73]</sup> The proton exchange membrane (PEM) in between the compartments is crucial to prevent gas mixing between O<sub>2</sub> and H<sub>2</sub>, which can form extremely dangerous knallgas mixtures (oxyhydrogen). The working principle of the DS-PEC is analogous to DSSC following the same electron propagation steps. Hence, the problems that arise due to recombination events in DSSCs also translate to the DS-PEC, but in a more severe way, as the catalyst also plays a role in the latter. Recombination events lead to losses in voltage ( $V_{OC}$ ), which hampers voltage depended electrocatalysis in the cell. The minimal voltage to drive a reaction is determined by the thermodynamic potential. A good catalyst operates close to this thermodynamic potential i.e., the catalyst should have a low overpotential to minimize potential losses and maximize solar to fuel efficiencies. Next to this, the time scales of events differ tremendously, as light absorption (fs) electron transfer (ps–ns) and catalysis ( $\mu$ s–ms) are orders of magnitude apart. Catalysis involves multiple steps, while only one electron is involved in photoinduced electron transfer. Therefore, all components and their intermediates must be sufficiently stable to deal with this time delay issue while recombination must be prevented.

As the recombination problems in the DSSC will only be amplified in a DS-PEC, this issue must be first addressed in DSSCs. Specifically, recombination in *p*-type hampers the design of functioning tandem devices, which precludes the translation of tandem DSSCs into DS-PECs. Therefore, the focus of the next section is to expose the issues in *p*-DSSCs in depth.

### 3.7 Exposing recombination issues in *p*-type DSSC

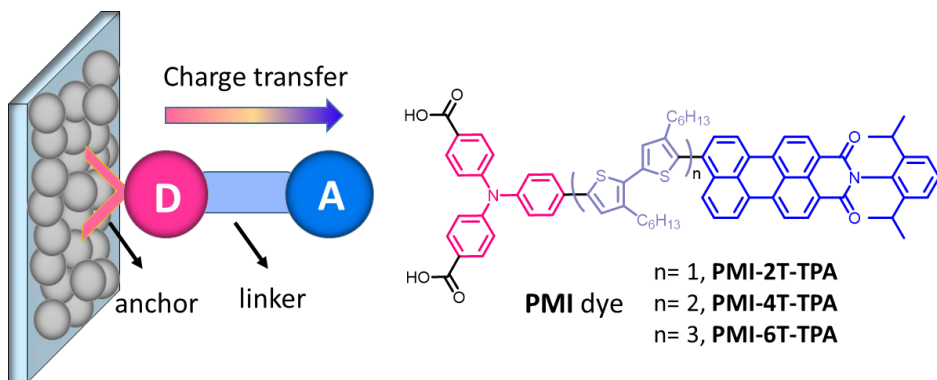
The origins of the dominant recombination pathways in *p*-DSSC have been studied with various techniques to uncover the processes occurring at the dye–semiconductor (D|NiO) interface at different timescales.<sup>[31]</sup> Transient absorption spectroscopy (TAS) and time resolved infrared (TRIR) techniques have been applied to study the ultrafast dynamics of excited dye relaxation and electron–hole recombination in the device (Figure 7). The charge

injection ( $\tau_{inj}$ ) from the VB into the dye typically takes place between 100 fs–100 ps, creating  $D^{\cdot-} | NiO^+$  relatively fast. Recombination from  $D^{\cdot-} | NiO^+$  occurs at the ps–ns timescale (typically  $\tau_{rec} < 1$  ns), which is also competing with dye regeneration.<sup>[64,74]</sup> There are cases in which dye regeneration is even slower than recombination leading to DSSC with low PCE.<sup>[75]</sup> TRIR has been employed to study changes in the electronic structure of the NiO bound dye upon excitation.<sup>[76–78]</sup> The characteristic carbonyl IR absorption from the carboxylate anchoring group of the dye shows a change in binding strength upon photon absorption and subsequent hole injection. For example, the benchmark **P1** dye (Figure 7) shows rapid hole injection ( $\tau_{inj} < 1$  ps), however, the charge separated lifetime was also found to be short (as  $\tau_{rec} < 1$  ns).<sup>[67]</sup> In *n*-DSSC the electron injection also occurs at the fs–ps timescale, but recombination takes place at a timescale that is 3 to 6 orders of magnitude slower, i.e. ms in *n*-DSSC compared to ns– $\mu$ s in *p*-DSSC.<sup>[64]</sup>



**Figure 7.** Energy diagram of the components within the DSSC including the relevant timescales of the forward electron propagation steps in blue (Dye excitation  $D^* | NiO$ ; hole injection  $D^{\cdot-} | NiO^+$ ; dye regeneration  $D | RC$ ) and the backward processes in red (Dye relaxation;  $D^{\cdot-} | NiO^+$  recombination; redox mediator  $RC^{\cdot-} | NiO^+$  recombination) (left). Chemical structure of the benchmark **P1** dye (right).





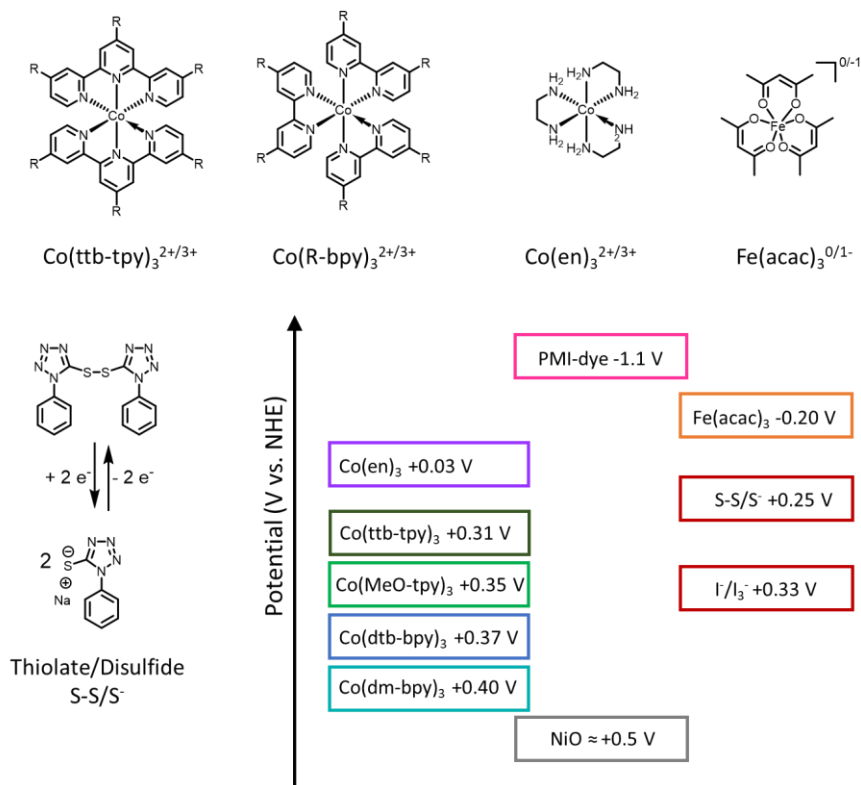
**Figure 8.** Schematic representation of a push–pull dye that is connected via an anchor to the NiO. Upon excitation, electron density from the HOMO is transferred to the acceptor side where the LUMO is located. The PMI dye series is an example of a push–pull dye where the donor triphenylamine (TPA, pink) is connected via a thiophene linker (T, violet) to the perylene diimide (PMI, blue) acceptor, which is the current efficiency record.<sup>[61]</sup>

Considerable effort has been made to enhance charge transfer within the device to address the fast recombination of  $D^+|NiO^+$ . This requires removal of the electron away from the semiconductor surface, therefore both dye and redox mediator play a key role in this. Research has mainly been focused on optimization of the individual components treating dye and redox mediators separately. For a well-functioning dye, it is expected that it should possess 1) a broad absorption across the visible–NIR region to capture the maximum amount of available sunlight, 2) a high molar absorption coefficient to capture the greatest amount of light with the thinnest possible layer to facilitate charge carrier transport with atom economy and 3) a suitable anchor to prevent dye leaching and promote device stability. Next, the HOMO/LUMO levels should promote efficient dye-to-semiconductor charge transfer, implying that the HOMO should be more negative than the level of the VB and the LUMO should be higher than the reduction potential of the redox mediator in *p*-DSSCs. To slow down recombination (Figure 6b, Process 6), people have employed push–pull dye designs, where the electron density is transferred to the periphery of the dye to localize the hole close to NiO for fast hole-injection. Localization of the electron density away from the NiO promotes fast dye regeneration to achieve a long-lived charge-separated state (Figure 8).<sup>[79]</sup> Equation 3 describes that electron transfer reactions become slower upon an increasing distance between D and A, according to Marcus theory.<sup>[22]</sup> This implies that the removal of electron density from the surface in  $D^+-A^-$ , causes charge recombination, the the resulting D–A species, is slow, a common applied strategy in preventing unwanted recombination.<sup>[26]</sup> TR spectroscopy generally supports that push–pull design leads to spatial separation of charges

between NiO and the dye and decreases  $\tau_{\text{rec}}$ , but this does not necessarily translate to improvements in the photovoltaic performance of the *p*-DSSC (Figure 8). This indicates a discrepancy between kinetics measured with TR techniques and what is actually happening in the actual device.

Despite the utilization of push-pull dyes hampering some of the recombination pathways, charge recombination is still an issue in the *p*-DSSC device. To understand this discrepancy, we should focus our attention on what is happening at the semiconductor-electrolyte interface. Transient photocurrent and photovoltage measurements in combination with electrical impedance measurements (EIS) were employed to uncover the processes taking place at the semiconductor-electrolyte interface. The principles of EIS are further discussed in Section 3.8. Elaborate analysis of transient photovoltage and EIS measurements showed a 1000-fold slower hole transport in NiO ( $4 \times 10^{-8} \text{ cm}^2 \text{ s}^{-1}$ )<sup>[62]</sup> compared to the  $(10^{-4} \text{ cm}^2 \text{ s}^{-1})$ <sup>[63]</sup> electron diffusion in TiO<sub>2</sub>. The limited hole mobility (1000-fold slower) within NiO compared to  $\text{TiO}_2$ , causes the extremely fast recombination in *p*-DSSC (ns- $\mu$ s) compared to *n*-DSSC (ms).<sup>[64,80]</sup> Fast electron transfer from the dye to the redox mediator is essential to compete with  $\tau_{\text{rec}}$  and good electronic overlap between D<sup>•</sup> and mediator is therefore crucial to promote electron transfer. Typically, the iodide/triiodide couple (I<sup>-</sup>/I<sub>3</sub><sup>-</sup>) is used, by mixing I<sub>2</sub> and LiI in MeCN. However, the small difference in potential of the I<sup>-</sup>/I<sub>3</sub><sup>-</sup> couple (0.33 V vs. NHE) and the Fermi level of NiO ( $\approx 0.5 \text{ V}$  vs. NHE) only allows for very low maximum  $V_{\text{OC}}$ . This is further explained in Box 4. Implementation of alternative redox couples with more negative redox potential should lead to higher  $V_{\text{OC}}$  to ultimately increase the PCE. Redox couples based on cobalt polypyridyl complexes proved to be effective in increasing the  $V_{\text{OC}}$  from 100 mV to 200–300 mV vs. NHE.<sup>[81]</sup> However, these mediators only work in combination with dyes that exhibit long-lived charge separated lifetimes (typically 5  $\mu$ s vs. 20 ps for **P1**), often very intricately designed molecules requiring long synthetic routes. Alternatively, organic redox mediators based on thiolate/disulfide developed by Bach and coworkers (Figure 9) have been applied to explore their use in DSSCs as high potential redox couple.<sup>[82]</sup> This electrolyte consisted of 5,5'-dithiobis(1-phenyl-1*H*-tetrazole) and sodium 1-phenyl-1*H*-tetrazole-5-thiolate, possessing a 70 mV more negative redox potential (245 mV vs. NHE). This electrolyte system was applied in combination with the **PMI** dye which gave a moderate  $V_{\text{OC}}$  enhancement of 60 mV (285 mV compared to 226 mV when the iodide/triiodide (I<sup>-</sup>/I<sub>3</sub><sup>-</sup>) couple is used. The **PMI** dye in combination with Fe(acac)<sub>3</sub> is the current record holder having a  $V_{\text{OC}}$  of 645 mV (compared to 243 mV of the **PMI** dye with I<sup>-</sup>/I<sub>3</sub><sup>-</sup> electrolyte) and  $J_{\text{sc}}$  is 7.65 mA cm<sup>-2</sup> leading to 2.51 % PCE.<sup>[61]</sup> For the sake of

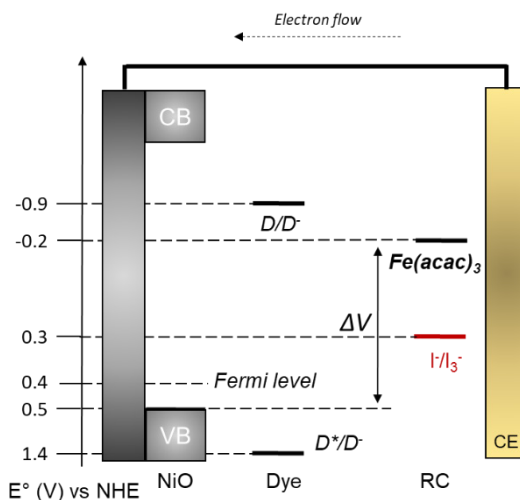
comparison, the best performing *n*-DSSC exhibits a  $V_{OC}$  of 1.013 V together with  $J_{SC}$  of 18.36 mA cm<sup>-2</sup> resulting in an almost 6 times higher PCE (14.3 %).<sup>[59]</sup>



**Figure 9.** Reduction potential of different redox mediators used in *p*-DSSCs in comparison with the HOMO level of the best performing PMI dye and the VB of NiO. This shows that  $\text{I}^-/\text{I}_3^-$  allows for low maximal potentials (difference between redox potential mediator and VB NiO), unlike to metal complexes.

#### Box 4. What does “ $V_{OC}$ ” mean?

The meaning of the  $V_{OC}$  can be understood as the maximum voltage of the device and that is achieved at open circuit, which is at zero current (Box 3). In  $p$ -DSSCs, this voltage is determined by the difference in voltage between the redox potential of the redox mediator and the level of the valence band.<sup>[74,84]</sup> The theoretical voltage that can be reached by the cell increases if a redox mediator is applied with a more negative redox potential, as is illustrated in Figure 10. For  $I^-/I_3^-$  the theoretical  $V_{OC}$  in a NiO  $p$ -DSSC is therefore 0.2 V while if the  $Fe(acac)_3$  this is much higher (0.7 V).<sup>[61]</sup> It is important to note that the theoretical  $V_{OC}$  is not determined by the HOMO or LUMO levels of the dye but solely by the chosen redox mediator together with the semiconductor. Deviation from the theoretical  $V_{OC}$  (i.e., voltage losses) in real devices originate from device imperfections that are discussed in Section 3.7. Imperfections in the semiconductor leads to an increase in Fermi level. The Fermi level is a material characteristic describing the amount of work that is required to add an electron. Charge flow through the semiconductor is highly influenced by the position of the Fermi level.<sup>[27]</sup>



**Figure 10.** Relative energy levels of a hypothetical  $p$ -DSSC employing dye D with either the  $I^-/I_3^-$  electrolyte or the  $Fe(acac)_3$  electrolyte.<sup>[61]</sup>

#### 3.8. Electrical Impedance Measurements for photoelectrochemical devices

Electrical impedance spectroscopy (EIS) specifically measures the frequency response of an electrochemical system in terms of energy storage (capacitance,  $C$ ) and energy dissipation (resistance,  $R$ ) upon application of an alternating voltage ( $V_{ac}$ ). The system is perturbed by a varying the frequency of  $V_{ac}$  while recording the alternating current response ( $I_{ac}$ ). As the perturbation input signal is small, the system under study is not changed irreversibly. It simply

relaxes to its equilibrium state, making EIS a non-destructive method. By studying photoelectrochemical devices interacting with electromagnetic fields enables the unravelling of fundamental events taking place within these systems. EIS is therefore a powerful method for power conversion technologies and finds applications in photovoltaic (PV) devices, organic photovoltaics (OPV) and dye-sensitized solar cells (DSSC).

### 3.8.1. Basics of Impedance

Impedance can be viewed as an extension on Ohm's law (Equation 5) describing the relationship of voltage ( $V$ ) to a direct current ( $I$ ) passing through a resistor ( $R$ ).

$$V = I R \quad (5)$$

Impedance, often denoted as  $Z$ , can be considered as a resistance to an alternating current circuit by applying an oscillating voltage.

$$V = I Z \quad (6)$$

This oscillating voltage can be described by Equation 7, where  $\phi$  is the angular frequency ( $\phi = 2 \pi f$ ).

$$V(t) = V_0 \sin(\omega t) \quad (7)$$

The current response of the system to the oscillating voltage will be shifted in phase  $\Phi$  from the applied signal (Equation 8). This shift in current is caused by the reactance due to capacitance or induction of the system.

$$I(t) = I_0 \sin(\omega t + \phi) \quad (8)$$

Euler's formula allows to rewrite Equation 6 and 7 (trigonometric functions) as complex exponential functions (Equation 9) where  $i = \sqrt{-1}$ .

$$e^{i\phi} = \cos \phi + i \sin \phi \quad (9)$$

Equation 10 is obtained by rewriting Equation 7 and 8 showing that impedance ( $Z$ ) is the ratio of an oscillating voltage to an oscillating current with phase angle  $\Phi$ . This is the polar coordinate representation.

$$Z = \frac{V(t)}{I(t)} = Z_0 e^{-i\phi} \quad (10)$$

Often impedance is written in Cartesian complex plane where the real and imaginary parts are divided (Equation 11).

$$Z = Z' - iZ'' \quad (11)$$

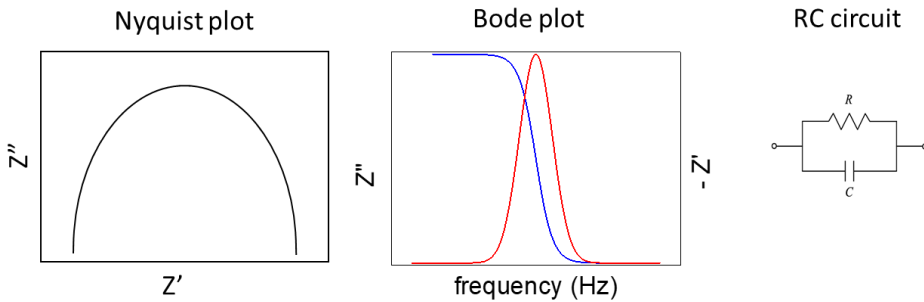
The real part represents the resistance (Equation 12).

$$Z' = Z_o \cos(-\phi) = \text{Resistance } R \quad (12)$$

The imaginary part represents the reactance (i.e., capacitance inductance) (Equation 13).

$$Z'' = Z_o \sin(-\phi) = \text{Reactance } X \quad (13)$$

By visualizing  $Z$  on a complex plane, the real part and complex part of the impedance can be plotted. This is the basis of the Nyquist plot where every point is a single frequency (Figure 11). The shape of the Nyquist plot might reveal what kind of system you are dealing with. The disadvantage of this way of representing is that there is no information on the phase angle and applied frequency. Therefore, the Nyquist plot is typically used in combination with the Bode plot where  $Z'$  and  $Z''$  are both represented as a function of frequency.


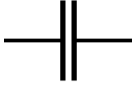


**Figure 11.** Nyquist plot (left) and Bode plot (middle) for a typical RC circuit (right). The maximum indicates  $\omega$  and  $f$ .

### 3.8.2. Impedance data interpretation

The most common method for analyzing impedance data is by composing equivalent circuit models. The circuit model is built from circuit elements as is represented in Table 1. A resistor is a circuit element that “resists” current flow through a circuit while all energy is dissipated. The impedance of a resistor is frequency independent contrary to the impedance of capacitors that vary inversely with frequency, while storing energy.

**Table 1.** Ideal circuit elements: resistor (R) and capacitor (C), together with their impedances.

| Element | Unit     | Symbol  | Z                           |
|---------|----------|---|-----------------------------|
| R       | $\Omega$ |  | $Z_R = R$                   |
| C       | F        |  | $Z_C = \frac{1}{i\omega C}$ |

If a process is modelled with a resistor and capacitor in parallel in a RC-circuit, we can see that at high frequency the impedance approximates the impedance belonging to a capacitor while at low frequency the impedance of the circuit is dominated by the resistor. The Nyquist plot shows the characteristic semicircle for a RC circuit (Figure 11). Typically, the shape of the Nyquist plot is characteristic for certain types or a combination of elements, which makes this method a fast strategy to look into the resistive and capacitive behavior of the system. When using this method, it is vital that the model corresponds to the actual physical events taking place within the device.

Different models have been developed to approximate several processes, such as carrier diffusion and recombination. In these equivalent circuit models, additional elements were introduced as the ideal circuit elements were non-applicable. In DSSCs ideal circuit elements are non-applicable, due to mass transport and non-homogeneous electrode surfaces. The nonhomogeneous working electrodes in DSSCs lead to inhomogeneous charge distribution at the electrode surface. Therefore, a constant phase element (CPE) is used to model the imperfect capacitor. Furthermore, mass transfer limitations can be modeled with a Warburg element. With these elements in hand, charge transfer at interfaces can be studied for DSSCs, which has led to the transmission line model by Bisquert and coworkers for example.<sup>[83]</sup> This model is widely used to describe diffusion and recombination processes and is commonly applied for DSSC technologies.<sup>[31]</sup>

#### 4. Supramolecular inspiration from Nature

The former part summarizes the considerable effort made over the past 20 years to increase the efficiency of *p*-DSSCs. However, to date, the performance is still subordinate to analogous *n*-DSSCs. When we focus on the properties of individual components, several parallels appear between the DSSC and PSII in natural photosynthesis. For example, both make use of chromophores for light absorption and redox mediators for charge transport. However, one significant difference is that the components of a DSSC have been optimized individually, without implementing interactions between elements, while in PSII all components cooperate for optimal performance. An example of this is the intricately designed **PMI** dye that makes use of an extended push-pull system (Figure 8), creating an extremely long charge separated state  $\tau(\text{NiO}^+ | \text{D}^-)$  of approximately 5  $\mu\text{s}$ . Hence, whenever a redox mediator molecule arrives by diffusing towards the dye electron transfer can take place. However, in PSII the kinetics of electron transfer steps between pigments are in the order of 100–300 ps instead, while still recombination is suppressed to a minimum.<sup>[85–87]</sup> This timescale difference can be explained by the structural organization that Nature employs to promote electron transfer (and energy transfer) between components that possess the right properties, such that transfer steps can be executed as efficiently as possible. Even the final electron acceptor  $\text{Q}_\text{B}$  (Figure 2), which is free to diffuse to the Q-pool, is also pre-organized in a pocket to accept charge. This level of molecular organization emphasizes the synergistic effect where all components are working together, contrasting the strategy employed in the former *p*-DSSC section, where components are treated as autonomous elements that make up the device. By promoting supramolecular interactions between the elements in the device, akin to PSII, the DSSC can benefit from enhancement in electron propagation to increase the efficiency in *p*-type DSSCs. Examples of supramolecular interactions for light harvesting and electrolyte pre-organization are known, although they are extremely rare. An overview of supramolecular interactions in DSSC is provided below.

##### 4.1 Supramolecular light harvesting in DSSCs

Nature employs supramolecular antennae as discussed in Section 2.1. Coutsolelos and co-workers showed that a hybrid artificial antenna system can be implemented as multichromophoric supramolecular assemblies in DSSCs.<sup>[88]</sup> This construct comprised of two types of porphyrins, a free base and a Zn analogue, bearing diphenylalanine units. The formation of the multi-molecular nanostructures occurs via H-bonds and the final assemblies show enhanced light absorption and light funneling. The PCE of the multichromophoric

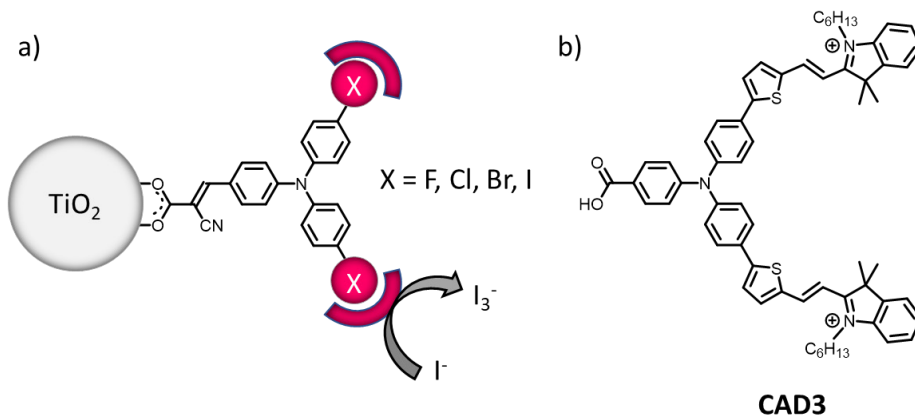


structure is higher (0.19%) than the individual porphyrin sensitizers (0.11%) although this performance remains low compared to other *n*-DSSC (PCE  $\approx$  14%).

#### 4.2 Dye–electrolyte interaction in DSSCs

Electron transfer between the redox mediator and the dye in current DSSC is purely collisional-based. Berlinguette and coworkers have studied the influence of supramolecular pre-organization of the electrolyte to the dye in *n*-DSSC (Figure 12).<sup>[89–91]</sup> In their device there is a halogen bond between the dye and the I<sup>-</sup>/I<sub>3</sub><sup>-</sup> electrolyte showing enhanced dye regeneration (Figure 6a, Process 3). The pre-organization of I<sup>-</sup> to the dye leads to higher PCE (6.5 %) compared to devices based on the [Co(bpy)<sub>3</sub>](PF<sub>6</sub>)<sub>3</sub> electrolyte (PCE = 5.4 %) that cannot interact with the dye. Furthermore, another study by Koumura and coworkers shows that a dye functionalized with a crown ether facilitates proximal pre-organization of Li<sup>+</sup> ions around the photosensitizer, with the local contraction of I<sup>-</sup>/I<sub>3</sub><sup>-</sup> resulting in less recombination in the *n*-DSSC.<sup>[92]</sup> The effects of pre-organization are small, resulting in little improvement of the PCE from 4.5% to 4.8% in presence of the interaction.

For *p*-DSSCs, the group of Gibson also present a system that is suspected to benefit from dye–mediator interactions.<sup>[93]</sup> This new **CAD3** dye is based on the benchmark **P1** dye with an improved push–pull system leading to higher PCEs (0.25 %) compared to **P1** with the iodide/triiodide couple (0.16 %, Figure 12b). The improved PCE is partly attributed to the better push–pull system promoting dye regeneration. Additionally, the cationic groups in **CAD3** can efficiently bind triiodide via ion–ion interactions, pre-organizing the redox acceptor and also promoting electron propagation.<sup>[76,77,93,94]</sup> Although the dye–I<sub>3</sub><sup>-</sup> interaction was not characterized, the authors hypothesized the better performance could partly be ascribed to this dye–mediator interaction.<sup>[76]</sup>



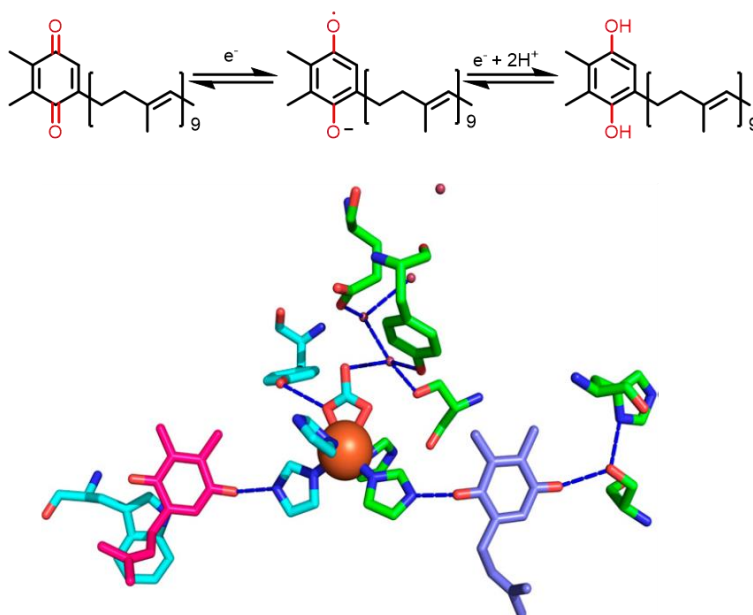
**Figure 12.** Systems that promote dye–mediator interactions for fast electron propagation. a) *n*-DSSC promoting halogen bonding between dye and mediator thereby pre-organizing the electron donor to the dye by Berlinguette and coworkers.<sup>[89–91]</sup> b) **CAD3** dye that possesses a positive charge to interact with the negatively charged triiodide electrolyte by Gibson *et al.*<sup>[76,93]</sup>

#### 4.3 Active removal of reduced redox mediators suppresses recombination in PSII

The four examples discussed above employ supramolecular chemistry to create interactions between the dye and redox mediator promoting electron transfer leading to increased PCEs for the DSSCs. Dye–mediator interaction seems to have a positive effect to counteract recombination analogous to pre-organization in PSII. By promoting electron transfer between the different components analogous to PSII, recombination Process 5 and 6 (Figure 6) can be partly addressed. Therefore, DSSCs are an excellent system to investigate how interactions between components create a synergistic effect in which the function of the device is better than predicted based on the sum of the properties of all components by using a systems approach.<sup>[55]</sup>

Quinones are the redox mediators within the photosynthetic apparatus as they connect three of the four complexes in the electron transfer chain, i.e., PSII, *cyt b<sub>6</sub>f* and PSI (Figure 2). Nature employs another strategy of preventing recombination by removing the final redox acceptor (Q<sub>B</sub>) away from PSII after reduction through the unbinding of QH<sub>2</sub> (Figure 2, Step 5). Q<sub>B</sub> interacts with the binding pocket of PSII via H-bonding with histidine and serine (Figure 13). After the second reduction QH<sub>2</sub> is formed that no longer forms H-bonds with serine and histidine, resulting in unbinding of QH<sub>2</sub> and diffusion into the thylakoid membrane, which takes 22 μs.<sup>[18]</sup> QH<sub>2</sub> is exchanged for a new quinone molecule that forms H-bonds with the

binding pocket ready to accept electrons. All in all, pre-organization of components and the final removal of QH<sub>2</sub> inhibits recombination in PSII.



**Figure 13.** Different oxidation states of quinone along with stick representation of the PSII acceptor side with Q<sub>A</sub> (pink) Q<sub>B</sub> (violet) interact via H-bonds (indicated by the blue dotted lines) with the protein environment. Data from the 1.9-Å structure (Protein Data Bank ID code 3WU2). This figure is adapted from Rutherford and coworkers.<sup>[17]</sup>

## 5. Machines working on the nanoscale

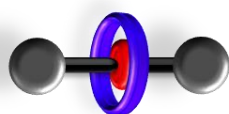
The last section mainly focused on the different PET steps within the photosynthetic apparatus, however, concurrently protons are released during these steps into the thylakoid lumen generating a proton gradient. This chemical gradient is ultimately used to create adenosine triphosphate (ATP) in the later stages of photosynthesis (Figure 2, Step 12). ATP is the fuel of life and is used in all chemical processes that are endergonic.

ATP is generated in an extraordinary process making use of a biological nanomachine called ATP-synthase.<sup>[95]</sup> In this process, a proton gradient is applied to drive this biological motor. By the rotating movement mechanical energy is transferred into chemical energy, which is used to fuse adenosine diphosphate (ADP) and inorganic phosphate (P<sub>i</sub>) into ATP. ATP synthase is found in all life forms powering all cellular activities. This nanosized machine is one of many in the human body. Next to ATP synthase other nanosized machines are

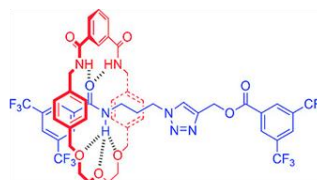
employed to induce molecular motion to move from one location to another with specialized motor proteins.<sup>[96]</sup> This molecular motion can be amplified to the macroscopic scale to contract muscles enabling us to walk and move around. These nanosized machines are the smallest machines known to exist and they are essential to life as they are involved in vital cellular tasks.

### 5.1 Molecular machines: setting molecules in motion

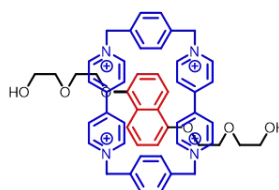
Inspired by Nature's array of motors and switches, chemists set out to develop artificial molecular machines (AMM). The relevance of this research area is clear from the 2016 Nobel prize awarded to Sauvage, Stoddart and Feringa for their contributions in the field of molecular machines.<sup>[97-99]</sup> Challenged by stimulus-responsive directional-motion, chemists have made amazing progress in this field by the development of molecular pumps<sup>[100,101]</sup>, propellers,<sup>[102,103]</sup> robotic arms<sup>[104]</sup>, synthetic ribosome<sup>[105]</sup> molecular muscles<sup>[106,107]</sup> and the nanocar<sup>[108]</sup>. Incorporating molecular machines and switches is the next step in miniaturization of devices.<sup>[109]</sup> The big challenge is to harness molecular motion in performing useful work to amplify work to a macroscopic level for signaling, communication and fuel generation for instance.<sup>[110]</sup>



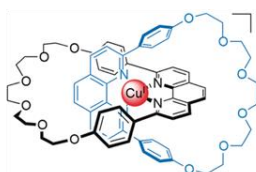
[2]Rotaxane



pseudorotaxane



[2]Catenane

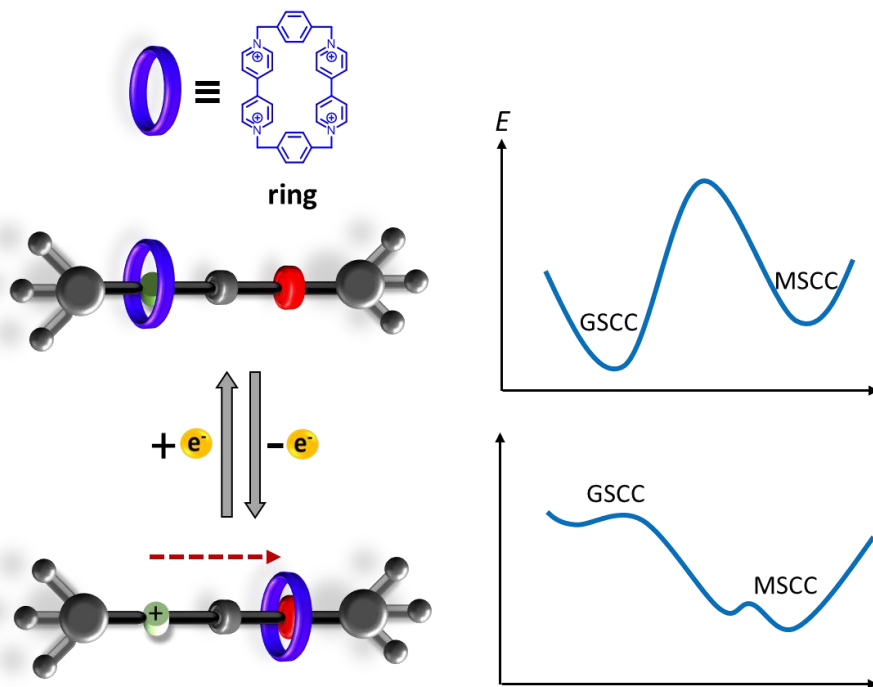


**Figure 14.** Rotaxane based on H-bonds; pseudorotaxane based on electron donor–acceptor interaction, catenane based on metal–ligand interaction.

Part of the molecular machine research field finds its origins within supramolecular chemistry.<sup>[111]</sup> The supramolecular bond is dynamic in its nature and allows for changes in molecular arrangement upon application of a chemical, electrochemical or photochemical stimulus, which is the fundament for molecular switches and machines. The first generation is based on mechanically interlocked molecules (MIMs). MIMs consist of at least two molecules that are not chemically, but mechanically bound together. Two different topologies are distinguished in which interlocked rings are called **catenanes** and if one ring is bound to a dumbbell shaped molecule it is called a **rotaxane** (Figure 14). It is an ideal platform to study switching between two states. For instance, the rotaxanes and pseudorotaxane systems designed by Stoddart, which consists of a macrocyclic ring that is bound to a thread (pseudorotaxane) or a thread with large stoppers at the end (rotaxane). Applying a (photo)chemical trigger enables the dethreading of a pseudorotaxane or switching stations in case of a rotaxane.<sup>[112,113]</sup> This switching behavior is the fundament of many molecular machines of which a small collection is presented below.

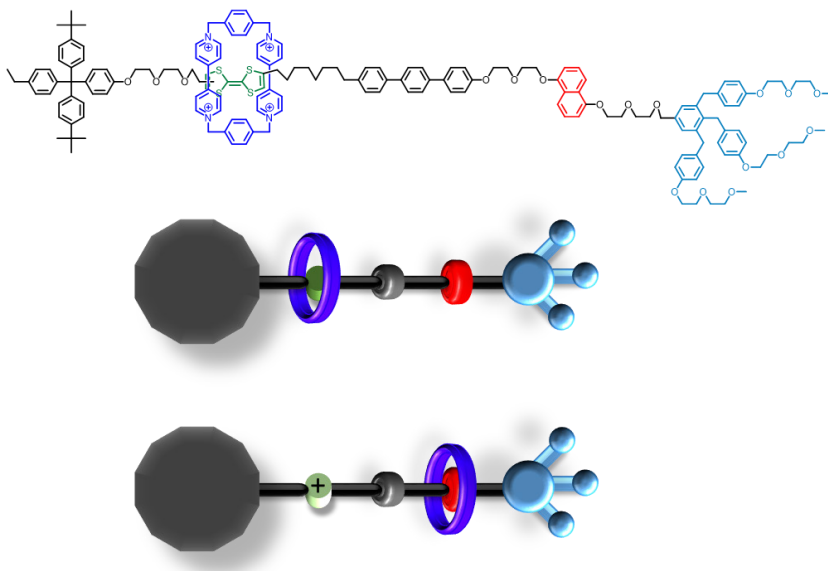
### *5.2. Redox driven switches*

The mechanical movement induced by an electrochemical trigger has been widely studied. The movement of the ring in MIMs can either be pirouetting or translational.<sup>[114-117]</sup> The pseudorotaxane represented in Figure 14 is a general structure for switching used in several applications. By addition of a second station on the thread, the ring can switch between these two stations (Figure 15). In the ground state co-conformation (GSCC) the ring resides around the green station while a small part of the population interacts with the red station, which is the metastable co-conformation (MSCC). Upon oxidation of the green station the positive charge repels the ring that unbinds and moves towards the red station. The MSCC is now lower in energy and the rotaxane effectively switched states.



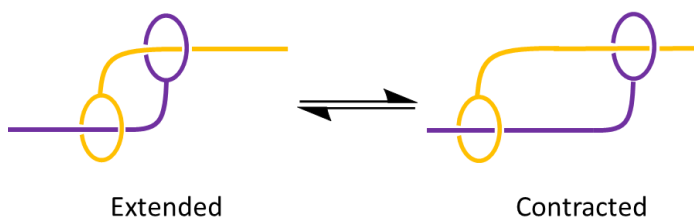
**Figure 15.** Switching of [2]rotaxanes that incorporate 2 recognition sites along with the energy profiles for redox driven switching.

This type of switchable rotaxane was immobilized as monolayer to function as data storage elements in which the state where the ring resided represented a “0” or a “1” (Figure 16).<sup>[118]</sup> These bits could be configured to comprise a fully dynamic function random access memory (DRAM) circuit that was able to receive and store information. Unfortunately, the circuit suffered from a large number of defects, but still it was a proof of principle of 160 Kbits installed in a  $10^{11}$  bits  $\text{cm}^{-2}$  configuration for molecular based DRAM.

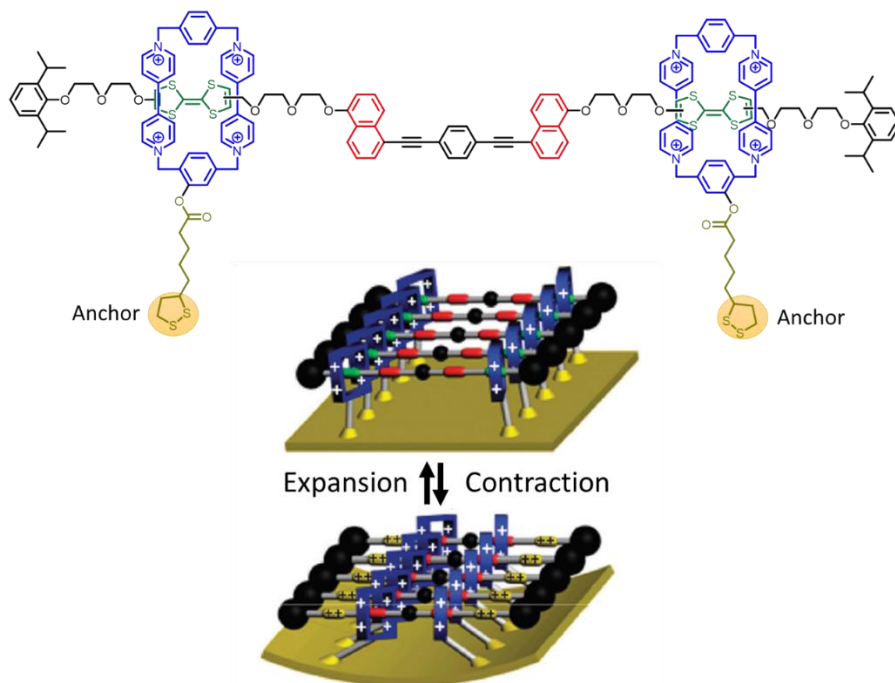


**Figure 16.** Molecular bits switching between two states “0” and “1”.

Switching of rotaxanes between two states is widely applicable. For example, if the switchable ring is connected to another element, strain could be induced. Inspired by myosin and actin found in the human body, chemist made their own artificial muscles.<sup>[96]</sup> In the human body muscles can contract because myosin moves over actin filaments causing strain fueled by ATP. By amplifying this molecular induced movement, it can be transferred into macroscopic motion. A daisy-chain topology is especially useful for contraction cycles (Figure 17),<sup>[119]</sup> Sauvage and coworkers synthesized rotaxanes with a daisy chain topology capable of contraction becoming 27% shorter.<sup>[106]</sup> In other work by Stoddart and coworkers, they used a different topology [3]rotaxane (Figure 18) that is connected to a gold film surface. Upon contraction this material bends caused by the 650 pN strength induced by rotaxane switching.<sup>[107,120]</sup>



**Figure 17.** Daisy chain topology in the extended and contracted configuration.

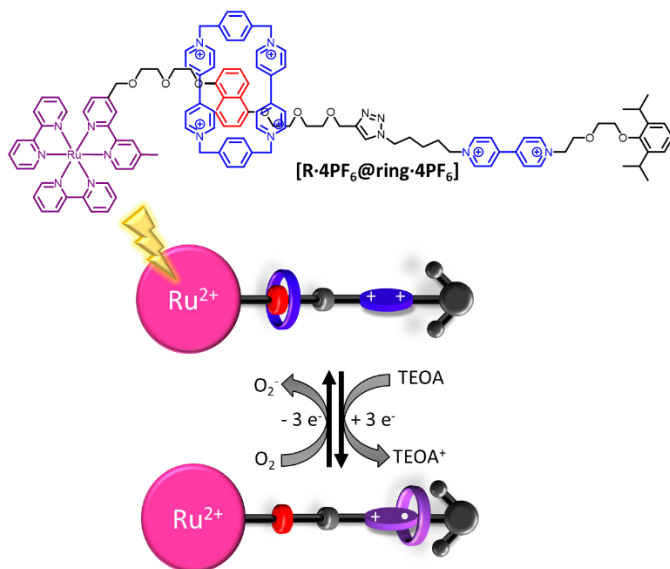


**Figure 18.** [3]Rotaxane immobilized on a substrate connected via rings. Upon oxidation the ring loses its affinity for the green station and moves to the **DNP** recognition site. By doing so, strain is induced in the material. Figure formatted from reference <sup>[107]</sup>.

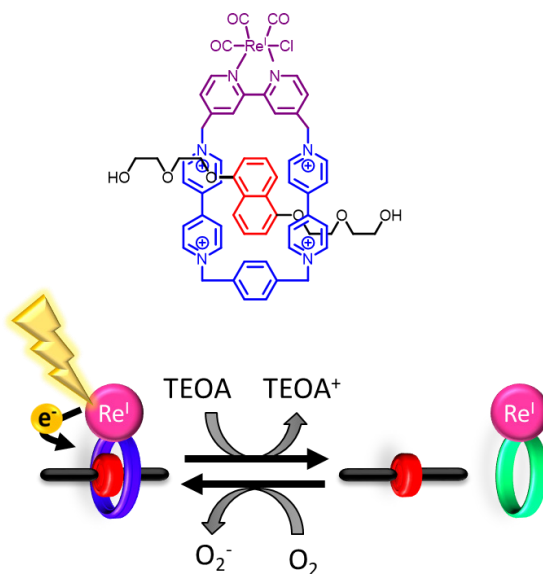
### 5.3. Photoredox driven switching

Rotaxanes with different stations can be switched by application of a (photo)chemical trigger.<sup>[112,113]</sup> Additionally, pseudorotaxane systems designed by Stoddart, stimulate the dethreading of the macrocycle after reduction of the ring breaking the supramolecular complex. The examples in Figure 19 and 20 show that upon reduction of the “blue box” the charged **ring** loses its affinity for the 1,5-dioxynaphthalene (**DNP**) recognition site (red).<sup>[112,121]</sup> This means that upon photoreduction the supramolecular complex between the ring and **DNP** is broken and the **ring** moves away. Hence, this **ring** can be considered as charge carrier capable of creating spatial separation of charges. Spatial charge separation is a fundamental step in artificial photosynthesis and molecular electronics, amongst others, and is therefore of great interest.<sup>[122,123]</sup>



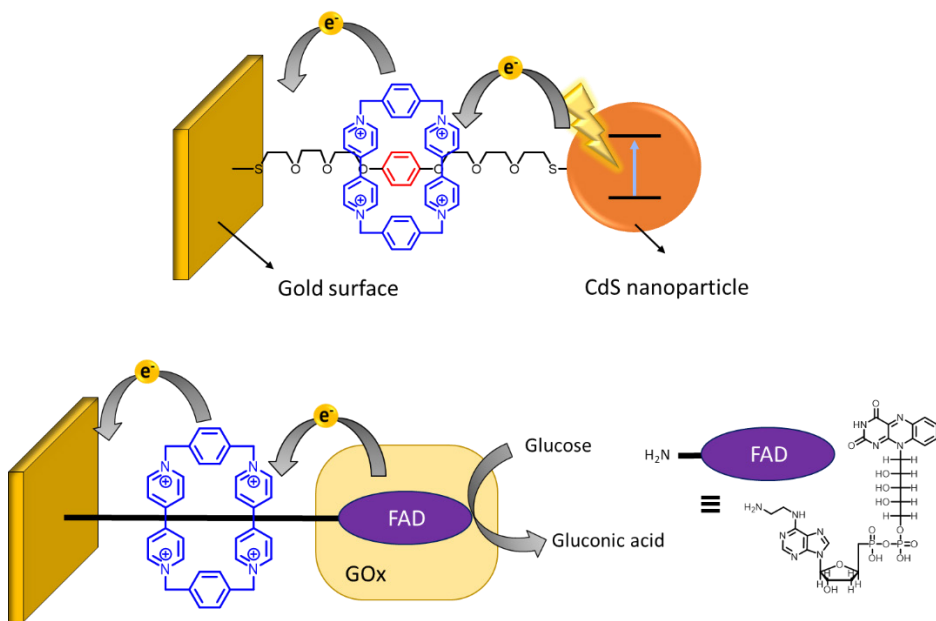


**Figure 19.** Light-stimulated switch based on a rotaxane consisting of two stations (**DNP** and methyl viologen (**MV**) recognition site) for the blue box **ring**. Upon excitation of the Ru<sup>2+</sup> photosensitizer the **ring** is reduced via PET and loses its affinity for the **DNP** recognition site. Reduction of the **MV**<sup>2+</sup> recognition site results in a radical-radical interacting complex between the **ring**<sup>2+2-</sup> and **MV**<sup>•+</sup>. Triethanolamine (TEOA) functions as a sacrificial electron donor and oxygen can be used to return to the starting state.<sup>[121]</sup>



**Figure 20.** The molecular piston by installing the Re<sup>+</sup> photosensitizer on the ring. Upon PET the ring loses its affinity for the **DNP** recognition site and the pseudorotaxane unbinds.<sup>[112]</sup>

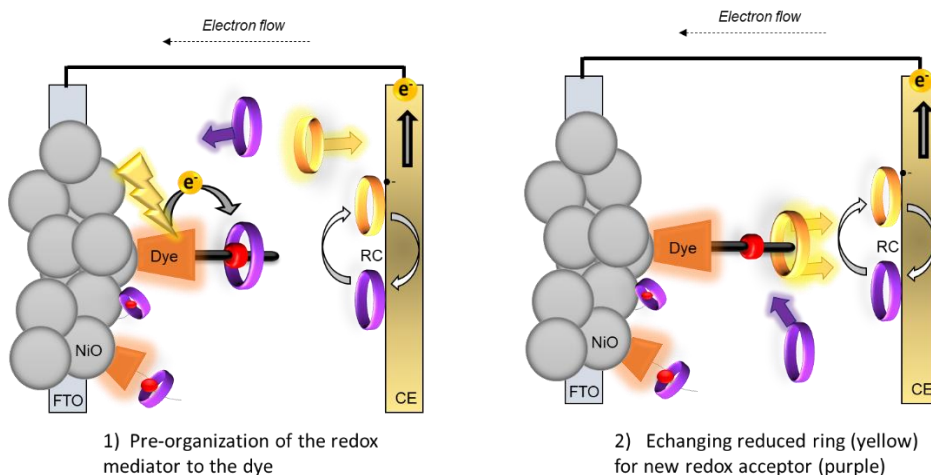
The charge transfer capabilities of the blue box **ring** were also demonstrated when immobilized as a rotaxane on a gold surface by Willner and coworkers.<sup>[124]</sup> They studied the electromechanics of the rotaxane consisting of **ring** on a molecular string, stoppered with an adamantane. They showed that in the ground state, the **ring** is bound to the diiminobenzene station, but when the **ring** is reduced, it unbinds and moves towards the gold electrode. In other work the adamantane stopper is replaced with CdS-nanoparticle (Figure 21).<sup>[125]</sup> This nanoparticle can be used in photochemical systems and upon excitation a photocurrent is generated. When integrated into a device, the **ring** is able to transfer an excited electron from the nanoparticle to the electrode leading to an 8 times higher photocurrent. The increase in photocurrent is explained by vectorial electron transfer from the nanoparticle to the **ring** creating a charge separated state. In other work the **ring**-based rotaxane is used to wire an enzyme to an electrode (Figure 21).<sup>[126]</sup> The enzyme glucose oxidase was fully functional while vectorial electron transfer was established from the enzyme towards the electrode via the rotaxane aiding the electric communication.



**Figure 21.** Different rotaxane systems on gold electrodes incorporating the blue box **ring** for vectorial electron transfer. By irradiating the CdS nanoparticle electrons are transferred to the ring bound to the 1,4-dihydroxybenzene recognition site. These electrons are then transferred to the gold electrode. Another example includes an enzymatic oxidation reaction. This rotaxane enzyme construct is self-assembled onto a gold surface similar to the CdS nanoparticle system. The *apo*-enzyme is added to the FAD connected rotaxane. This enzyme oxidizes glucose to gluconic acid. Vectorial electron transfer from the enzyme through the ring to the gold surface is achieved.

## 6. The aim of Part B

The field of *p*-DSSC is challenged by low efficiencies caused by low hole mobility in the NiO semiconductor enhancing recombination pathways. To battle charge recombination, this thesis seeks to use a holistic approach emphasizing on the crucial interactions between components to favor electron propagation within the device. Natural photosynthesis uses supramolecular organization to achieve efficient charge transfer and pre-organization of the final  $Q_B$  acceptor that is exchanged after double reduction to generate  $QH_2$ , for a new quinone. In this part we aim to address recombination issues hampering *p*-DSSC using supramolecular machines inspired by binding and unbinding events of quinone found in PSII (Figure 22). To promote binding and unbinding events molecular machines are proposed (introduced in Section 5.2.), where rings lose their affinity for the binding site upon reduction acting as a macrocyclic charge carrier (Figure 22). In our design the redox mediator interacts with a recognition site that is connected to a molecular dye. After PET from the dye, we envision that the redox mediator unbinds, caused by repulsion, creating a charge separated state. In this case, the reduced mediator is the charge carrier that moves away from the D|NiO surface, ultimately suppressing recombination pathways 5 and 6 (Figure 6b).



**Figure 22.** Design for addressing recombination issues in *p*-DSSC with a biomimetic approach inspired by PSII. The redox mediator (purple) is macrocyclic redox acceptor that is able to interact with the binding site (red). The redox mediator is thereby pre-organized to the dye (orange) that is chemisorbed to the NiO nanoparticles. Upon excitation of the dye an electron is transferred via PET from the dye to the redox mediator. The reduced acceptor (yellow) no longer has an interaction with the red binding site on the dye and is swapped from a new purple acceptor by unbinding. The reduced redox mediator diffuses towards the counter electrode where it gets regenerated. This design uses two strategies from PSII. 1) Pre-organizing the redox acceptor to the electron donating dye. 2) Swapping reduced redox acceptors for new redox acceptor akin to  $Q_B$  and  $QH_2$  in PSII. FTO = fluorine-doped tin oxide, RC = redox couple, CE = counter electrode.

The research question that this part of the thesis seeks to answer is:

*“Can we use molecular machinery to suppress recombination in *p*-DSSC to enhance their efficiency?”*

**Chapter 5** describes the first-generation of *p*-DSSC based on molecular machines, where the viologen based “blue box” **ring** is employed as redox mediator that binds to a molecular dye. This **P<sub>STATION</sub>** dye is functionalized with the **DNP** recognition site to form pseudorotaxanes with tetracationic **ring**. The pseudorotaxane based DSSC shows a 10 times enhancement in photocurrent, compared to analogous systems that do not exploit pseudorotaxane formation. Although this system is limited in its performance in terms of PCE, it demonstrates a proof-of-principle that our concept of pseudorotaxane mediated charge transfer promotes forward electron propagation within *p*-DSSCs.

**Chapter 6** describes the 2<sup>nd</sup> generation with a neutral naphthalene diimide based ring (**3-NDI-ring**) overcoming the low PCEs found in Chapter 5. Ring binding and launching demonstrates that integration of molecular machinery is a viable strategy to promote charge rectification. The inhibition of recombination was characterized by a two times increase in hole lifetime leading to a higher  $V_{OC}$  and  $J_{SC}$  resulting in a 5 times higher PCE.

**Chapter 7** focusses on a closer mimic to PSII where one mediator is permanently bound to the **P<sub>Rotaxane</sub>** dye while free diffusing mediators can still interact with the second **DNP** unit. The dynamic mediator binds in the oxidized form and unbinds upon reduction. The **3-NDI-ring-P<sub>Rotaxane</sub>** system shows suppression of charge recombination leading to 16 times longer hole lifetimes compared to the analogues based on  $I^-/I_3^-$  electrolyte. The **3-NDI-ring-P<sub>Rotaxane</sub>** system outperforms  $I^-/I_3^-$  systems by a twofold increase in PCE, despite the 40 times lower electrolyte concentration. However, photocurrents are still 4 times lower compared to devices based on the  $I^-/I_3^-$  electrolyte and this is attributed to slow diffusion. This diffusion limitation is further investigated with EIS to confirm this being the major issue while recombination is inhibited to a minimum in the mediator launching devices.

## References

- [1] R. Perez, M. Perez, *IEA SHC Sol. Updat.* **2015**, *62*, 4–6.
- [2] “Our World in Data,” can be found under <https://ourworldindata.org/energy-mix>, **2019**.
- [3] BP, “BP Statistical Review of World Energy 2020,” **2020**.
- [4] IEA, “Global Energy Review 2019,” can be found under <https://www.iea.org/reports/global-energy-review-2019>, **2019**.
- [5] N. S. Lewis, D. G. Nocera, *Proc. Natl. Acad. Sci.* **2006**, *103*, 15729–15735.
- [6] R. Croce, H. Van Amerongen, *J. Photochem. Photobiol. B Biol.* **2011**, *104*, 142–153.
- [7] J. Barber, B. Andersson, *Nature* **1994**, *370*, 31–34.
- [8] H. Dau, I. Zaharieva, *Acc. Chem. Res.* **2009**, *42*, 1861–1870.
- [9] A. Magnuson, M. Anderlund, O. Johansson, P. Lindblad, R. Lomoth, T. Polivka, S. Ott, K. Stensjö, S. Styring, V. Sundström, L. Hammarström, *Acc. Chem. Res.* **2009**, *42*, 1899–1909.
- [10] J. M. Berg, J. L. Tymoczko, L. Stryer, *Biochemistry*, W. H. Freeman And Company, New York, **2007**.
- [11] B. Wardle, *Principles and Applications of Photochemistry*, John Wiley & Sons, Ltd, Chichester, **2009**.
- [12] A. S. K. Sun, K. Sauer, *Biochim. Biophys. Acta - Bioenerg.* **1971**, *234*, 399–414.
- [13] G. S. Beddard, G. Porter, *Nature* **1976**, *260*, 366–367.
- [14] R. Croce, H. van Amerongen, *Nat. Chem. Biol.* **2014**, *10*, 492–501.
- [15] K. M. Smith, L. A. Kehres, J. Fajer, *J. Am. Chem. Soc.* **1983**, *105*, 1387–1389.
- [16] F. Würthner, T. E. Kaiser, C. R. Saha-Möller, *Angew. Chemie Int. Ed.* **2011**, DOI 10.1002/anie.201002307.
- [17] S. De Causmaecker, J. S. Douglass, A. Fantuzzi, W. Nitschke, A. W. Rutherford, *Proc. Natl. Acad. Sci.* **2019**, *116*, 19458–19463.
- [18] F. J. Van Eerden, M. N. Melo, P. W. J. M. Frederix, X. Periole, S. J. Marrink, *Nat. Commun.* **2017**, *8*, 1–8.
- [19] M. Lambrev, D. Russo, F. Polticelli, V. Scognamiglio, A. Antonacci, V. Zobnina, G. Campi, G. Rea, *Curr. Protein Pept. Sci.* **2014**, *15*, 285–295.
- [20] H. Ishikita, K. Hasegawa, T. Noguchi, *Biochemistry* **2011**, *50*, 5436–5442.
- [21] H. Makita, G. Hastings, *Proc. Natl. Acad. Sci.* **2017**, *114*, 9267–9272.
- [22] A. O. Cohen, R. A. Marcus, *J. Phys. Chem.* **1968**, *72*, 4249–4256.
- [23] J. L. Sessler, A. Hardman, B. Wang, *J. Am. Chem. Soc.* **1993**, 10418–10419.
- [24] N. L. Bill, O. Trukhina, J. L. Sessler, T. Torres, *Chem. Commun.* **2015**, *51*, 7781–7794.
- [25] J. M. Artés, I. Diez-Pérez, F. Sanz, P. Gorostiza, *ACS Nano* **2011**, *5*, 2060–2066.
- [26] G. García, C. Adamo, I. Ciofini, *Phys. Chem. Chem. Phys.* **2013**, *15*, 20210.
- [27] M. Pazoki, U. B. Cappel, E. M. J. Johansson, A. Hagfeldt, G. Boschloo, *Energy Environ. Sci.* **2017**, *10*, 672–709.
- [28] H. J. Snaith, *Nat. Photonics Photonics* **2012**, *6*, 337–340.
- [29] X. Yang, M. Yanagida, L. Han, *Energy Environ. Sci.* **2013**, *6*, 54–66.
- [30] J. Halme, P. Vahermaa, K. Miettunen, P. Lund, *Adv. Mater.* **2010**, *22*, 210–234.
- [31] E. Benazzi, J. Mallows, G. H. Summers, F. A. Black, E. A. Gibson, *J. Mater. Chem. C* **2019**, *7*, 10409–10445.
- [32] K. Takagi, S. Magaino, H. Saito, T. Aoki, D. Aoki, *J. Photochem. Photobiol. C* **2013**, *14*, 1–12.
- [33] P. R. F. Barnes, K. Miettunen, X. Li, A. Y. Anderson, T. Bessho, M. Grätzel, B. C. O’Regan, *Adv. Mater.* **2013**, *25*, 1881–1922.
- [34] R. Katoh, A. Furube, *J. Photochem. Photobiol. C Photochem. Rev.* **2014**, *20*, 1–16.
- [35] E. von Hauff, *J. Phys. Chem. C* **2019**, *123*, 11329–11346.
- [36] F. Fabregat-Santiago, G. Garcia-Belmonte, I. Mora-Sero, J. Bisquert, *Phys. Chem. Chem. Phys.* **2011**, *13*, 9083–9118.
- [37] E. M. J. Johansson, R. Lindblad, H. Siegbahn, A. Hagfeldt, H. Rensmo, *ChemPhysChem* **2014**, *15*, 1006–1017.
- [38] T. Grube, J. Reul, M. Reuß, S. Calnan, N. Monnerie, R. Schlatmann, C. Sattler, M. Robinius, D. Stolten, *Sustain. Energy Fuels* **2020**, *4*, 5818–5834.
- [39] M. Reuß, J. Reul, T. Grube, M. Langemann, S. Calnan, M. Robinius, R. Schlatmann, U. Rau, D. Stolten, *Sustain. Energy Fuels* **2019**, *3*, 801–813.
- [40] E. Benazzi, J. Mallows, G. H. Summers, F. A. Black, E. A. Gibson, *J. Mater. Chem. C* **2019**, *7*,

10409–10445.

- [41] A. Kojima, K. Teshima, Y. Shirai, T. Miyasaka, *J. Am. Chem. Soc.* **2009**, *131*, 6050–6051.
- [42] J. Gong, S. B. Darling, F. You, *Energy Environ. Sci.* **2015**, *8*, 1953–1968.
- [43] D. Bryant, N. Aristidou, S. Pont, I. Sanchez-Molina, T. Chotchunangatchaval, S. Wheeler, J. R. Durrant, S. A. Haque, *Energy Environ. Sci.* **2016**, *9*, 1655–1660.
- [44] A. Babayigit, A. Ethirajan, M. Muller, B. Conings, *Nat. Mater.* **2016**, *15*, 247–251.
- [45] V. K. Ravi, B. Mondal, V. V. Nawale, A. Nag, *ACS Omega* **2020**, *5*, 29631–29641.
- [46] G. Peharz, F. Dimroth, U. Wittstadt, *Int. J. Hydrogen Energy* **2007**, *32*, 3248–3252.
- [47] J. Jia, L. C. Seitz, J. D. Benck, Y. Huo, Y. Chen, J. W. D. Ng, T. Bilir, J. S. Harris, T. F. Jaramillo, *Nat. Commun.* **2016**, *7*, 13237.
- [48] A. V. Akimov, A. J. Neukirch, O. V. Prezhdo, *Chem. Rev.* **2013**, *113*, 4496–4565.
- [49] D. G. Nocera, *Acc. Chem. Res.* **2012**, *45*, 767–776.
- [50] A. Fujishima, K. Honda, *Nature* **1972**, *238*, 37–38.
- [51] T. Hisatomi, K. Domen, *Nat. Catal.* **2019**, *2*, 387–399.
- [52] Y.-W. Su, S.-C. Lan, K.-H. Wei, *Mater. Today* **2012**, *15*, 554–562.
- [53] H. Hoppe, N. S. Sariciftci, *J. Mater. Res.* **2004**, *19*, 1924–1945.
- [54] R. Bhosale, J. Mišek, N. Sakai, S. Matile, *Chem. Soc. Rev.* **2010**, *39*, 138–149.
- [55] F. Würthner, K. Meerholz, *Chem. Eur. J.* **2010**, *16*, 9366–9373.
- [56] A. Distler, C. J. Brabec, H. Egelhaaf, *Prog. Photovoltaics Res. Appl.* **2021**, *29*, 24–31.
- [57] X. Huang, B. Sun, Y. Li, C. Jiang, D. Fan, J. Fan, S. R. Forrest, *Appl. Phys. Lett.* **2020**, *116*, 153501.
- [58] B. O'Regan, M. Grätzel, *Nature* **1991**, *353*, 737–740.
- [59] K. Kakiage, Y. Aoyama, T. Yano, K. Oya, J. Fujisawa, M. Hanaya, *Chem. Commun.* **2015**, *51*, 15894–15897.
- [60] M. Freitag, J. Teuscher, Y. Saygili, X. Zhang, F. Giordano, P. Liska, J. Hua, S. M. Zakeeruddin, J. E. Moser, M. Grätzel, A. Hagfeldt, *Nat. Photonics* **2017**, *11*, 372–378.
- [61] I. R. Perera, T. Daeneke, S. Makuta, Z. Yu, Y. Tachibana, A. Mishra, P. Bäuerle, C. A. Ohlin, U. Bach, L. Spiccia, *Angew. Chemie Int. Ed.* **2015**, *54*, 3758–3762.
- [62] S. Mori, S. Fukuda, S. Sumikura, Y. Takeda, Y. Tamaki, E. Suzuki, T. Abe, *J. Phys. Chem. C* **2008**, *112*, 16134–16139.
- [63] S. Nakade, Y. Saito, W. Kubo, T. Kitamura, Y. Wada, S. Yanagida, *J. Phys. Chem. B* **2003**, *107*, 8607–8611.
- [64] A. Morandeira, G. Boschloo, A. Hagfeldt, L. Hammarström, *J. Phys. Chem. B* **2005**, *109*, 19403–19410.
- [65] T. Daeneke, Z. Yu, G. P. Lee, D. Fu, N. W. Duffy, S. Makuta, Y. Tachibana, L. Spiccia, A. Mishra, P. Bäuerle, U. Bach, *Adv. Energy Mater.* **2015**, *5*, 1401387.
- [66] J. He, H. Lindström, A. Hagfeldt, S. E. Lindquist, *Sol. Energy Mater. Sol. Cells* **2000**, *62*, 265–273.
- [67] A. Nattestad, M. Ferguson, R. Kerr, Y.-B. Cheng, U. Bach, *Nanotechnology* **2008**, *19*, 295304.
- [68] A. Fujishima, K. Honda, *Nature* **1972**, *238*, 37–38.
- [69] J. J. Leung, J. Warnan, K. H. Ly, N. Heidary, D. H. Nam, M. F. Kuehnel, E. Reisner, *Nat. Catal.* **2019**, *2*, 354–365.
- [70] T. E. Rosser, T. Hisatomi, S. Sun, D. Antón-García, T. Minegishi, E. Reisner, K. Domen, *Chem. – A Eur. J.* **2018**, *24*, 18393–18397.
- [71] W. Song, A. K. Vannucci, B. H. Farnum, A. M. Lapidus, M. K. Brennaman, B. Kalanyan, L. Alibabaei, J. J. Concepcion, M. D. Losego, G. N. Parsons, T. J. Meyer, *J. Am. Chem. Soc.* **2014**, *136*, 9773–9779.
- [72] D. F. Bruggeman, T. M. A. Bakker, S. Mathew, J. N. H. Reek, *Chem. – A Eur. J.* **2021**, *27*, 218–221.
- [73] C. Liu, B. C. Colón, M. Ziesack, P. A. Silver, D. G. Nocera, *Science* **2016**, *352*, 1210–1213.
- [74] F. Odobel, Y. Pellegrin, E. A. Gibson, A. Hagfeldt, A. L. Smeigh, L. Hammarström, *Coord. Chem. Rev.* **2012**, *256*, 2414–2423.
- [75] P. Qin, J. Wiberg, E. A. Gibson, M. Linder, L. Li, T. Brinck, A. Hagfeldt, B. Albinsson, L. Sun, *J. Phys. Chem. C* **2010**, *114*, 4738–4748.
- [76] F. A. Black, C. A. Clark, G. H. Summers, I. P. Clark, M. Towrie, T. Penfold, M. W. George, E. A. Gibson, *Phys. Chem. Chem. Phys.* **2017**, *19*, 7877–7885.
- [77] F. A. Black, C. J. Wood, S. Ngwerume, G. H. Summers, I. P. Clark, M. Towrie, J. E. Camp, E. A. Gibson, *Faraday Discuss.* **2017**, *198*, 449–461.
- [78] G. M. Greetham, D. Sole, I. P. Clark, A. W. Parker, M. R. Pollard, M. Towrie, *Rev. Sci.*

- Instrum.* **2012**, *83*, 103107.
- [79] J. F. Lefebvre, X. Z. Sun, J. A. Calladine, M. W. George, E. A. Gibson, *Chem. Commun.* **2014**, *50*, 5258–5260.
- [80] H. Zhu, A. Hagfeldt, G. Boschloo, *J. Phys. Chem. C* **2007**, *111*, 17455–17458.
- [81] E. A. Gibson, A. L. Smeigh, L. Le Pleux, L. Hammarstr, F. Odobel, G. Boschloo, A. Hagfeldt, **2011**, 9772–9779.
- [82] S. Powar, R. Bhargava, T. Daeneke, G. Götz, P. Bäuerle, T. Geiger, S. Kuster, F. A. Nüesch, L. Spiccia, U. Bach, *Electrochim. Acta* **2015**, *182*, 458–463.
- [83] F. Fabregat-Santiago, G. Garcia-Belmonte, I. Mora-Seró, J. Bisquert, *Phys. Chem. Chem. Phys.* **2011**, *13*, 9083–9118.
- [84] A. Hagfeldt, G. Boschloo, L. Sun, L. Kloo, H. Pettersson, *Chem. Rev.* **2010**, *110*, 6595–6663.
- [85] M. Grabolle, H. Dau, *Biochim. Biophys. Acta - Bioenerg.* **2005**, *1708*, 209–218.
- [86] A. R. Holzwarth, M. G. Müller, M. Reus, M. Nowaczyk, J. Sander, M. Rogner, *Proc. Natl. Acad. Sci.* **2006**, *103*, 6895–6900.
- [87] J. Buchta, M. Grabolle, H. Dau, *Biochim. Biophys. Acta - Bioenerg.* **2007**, *1767*, 565–574.
- [88] G. Charalambidis, K. Karikis, E. Georgilis, B. L. M'Sabah, Y. Pellegrin, A. Planchat, B. Lucas, A. Mitraki, J. Bouclé, F. Odobel, A. G. Coutsolelos, *Sustain. Energy Fuels* **2017**, *1*, 387–395.
- [89] F. G. L. Parlane, C. Mustoe, C. W. Kellett, S. J. Simon, W. B. Swords, G. J. Meyer, P. Kennepohl, C. P. Berlinguette, *Nat. Commun.* **2017**, *8*, 1–7.
- [90] S. J. C. Simon, F. G. L. Parlane, W. B. Swords, C. W. Kellett, C. Du, B. Lam, R. K. Dean, K. Hu, G. J. Meyer, C. P. Berlinguette, *J. Am. Chem. Soc.* **2016**, *138*, 10406–10409.
- [91] W. B. Swords, S. J. C. Simon, F. G. L. Parlane, R. K. Dean, C. W. Kellett, K. Hu, G. J. Meyer, C. P. Berlinguette, *Angew. Chem. Int. Ed.* **2016**, *55*, 5956–5960.
- [92] Y. Uemura, T. N. Murakami, N. Koumura, *J. Phys. Chem. C* **2014**, *118*, 16749–16759.
- [93] C. J. Wood, G. H. Summers, E. A. Gibson, *Chem. Commun.* **2015**, *51*, 3915–3918.
- [94] P. Qin, M. Linder, T. Brinck, G. Boschloo, A. Hagfeldt, L. Sun, *Adv. Mater.* **2009**, *21*, 2993–2996.
- [95] H. Itoh, A. Takahashi, K. Adachi, H. Noji, R. Yasuda, M. Yoshida, K. Kinoshita, *Nature* **2004**, *427*, 465–468.
- [96] G. Saper, H. Hess, *Chem. Rev.* **2020**, *120*, 288–309.
- [97] J.-P. Sauvage, *Angew. Chemie Int. Ed.* **2017**, *56*, 11080–11093.
- [98] J. F. Stoddart, *Angew. Chemie Int. Ed.* **2017**, *56*, 11094–11125.
- [99] B. L. Feringa, *Angew. Chemie Int. Ed.* **2017**, *56*, 11060–11078.
- [100] C. Cheng, P. R. McGonigal, S. T. Schneebeli, H. Li, N. A. Vermeulen, C. Ke, J. F. Stoddart, *Nat. Nanotechnol.* **2015**, *10*, 547–553.
- [101] K. Cai, Y. Shi, G. W. Zhuang, L. Zhang, Y. Qiu, D. Shen, H. Chen, Y. Jiao, H. Wu, C. Cheng, J. F. Stoddart, J. F. Stoddart, J. F. Stoddart, *J. Am. Chem. Soc.* **2020**, *142*, 10308–10313.
- [102] C. D. Simpson, G. Mättersteig, K. Martin, L. Gherghel, R. E. Bauer, H. J. Räder, K. Müllen, *J. Am. Chem. Soc.* **2004**, *126*, 3139–3147.
- [103] A. M. Fennimore, T. D. Yuzvinsky, W.-Q. Han, M. S. Fuhrer, J. Cumings, A. Zettl, *Nature* **2003**, *424*, 408–410.
- [104] S. Kassem, A. T. L. Lee, D. A. Leigh, A. Markevicius, J. Solà, *Nat. Chem.* **2016**, *8*, 138–143.
- [105] B. Lewandowski, G. De Bo, J. W. Ward, M. Pappmeyer, S. Kuschel, M. J. Aldegunde, P. M. E. Gramlich, D. Heckmann, S. M. Goldup, D. M. D'Souza, A. E. Fernandes, D. a. Leigh, *Science* **2013**, *339*, 189–193.
- [106] M. C. Jiménez, C. Dietrich-Buchecker, J. Sauvage, *Angew. Chemie* **2000**, *39*, 3284–3287.
- [107] B. K. Juluri, A. S. Kumar, Y. Liu, T. Ye, Y. W. Yang, A. H. Flood, L. Fang, J. F. Stoddart, P. S. Weiss, T. J. Huang, *ACS Nano* **2009**, *3*, 291–300.
- [108] T. Kudernac, N. Ruangsupapichat, M. Parschau, B. MacLá, N. Katsonis, S. R. Harutyunyan, K. H. Ernst, B. L. Feringa, *Nature* **2011**, *479*, 208–211.
- [109] J. J. Davis, G. A. Orlowski, H. Rahman, P. D. Beer, *Chem. Commun.* **2010**, *46*, 54–63.
- [110] I. Aprahamian, *ACS Cent. Sci.* **2020**, *6*, 347–358.
- [111] J. M. Lehn, *Chem. Soc. Rev.* **2007**, *36*, 151–160.
- [112] P. R. Ashton, V. Balzani, O. Kocian, L. Prodi, N. Spencer, J. F. Stoddart, *J. Am. Chem. Soc.* **1998**, *120*, 11190–11191.
- [113] S. Saha, E. Johansson, A. H. Flood, H.-R. Tseng, J. I. Zink, J. F. Stoddart, *Chem. Eur. J.* **2005**, *11*, 6846–6858.

- [114] I. Poleschak, J.-M. Kern, J.-P. Sauvage, *Chem. Commun.* **2004**, 474.
- [115] A. C. Fahrenbach, C. J. Bruns, D. Cao, J. F. Stoddart, *Acc. Chem. Res.* **2012**, *45*, 1581–1592.
- [116] J. W. Choi, A. H. Flood, D. W. Steuerman, S. Nygaard, A. B. Braunschweig, N. N. P. Moonen, B. W. Laursen, Y. Luo, E. Delonno, A. J. Peters, J. O. Jeppesen, K. Xu, J. F. Stoddart, J. R. Heath, *Chem. Eur. J.* **2006**, *12*, 261–279.
- [117] A. C. Fahrenbach, C. J. Bruns, H. Li, A. Trabolsi, A. Coskun, J. F. Stoddart, *Acc. Chem. Res.* **2014**, *47*, 482–493.
- [118] J. E. Green, J. Wook Choi, A. Boukai, Y. Bunimovich, E. Johnston-Halperin, E. DeIonno, Y. Luo, B. A. Sheriff, K. Xu, Y. Shik Shin, H.-R. Tseng, J. F. Stoddart, J. R. Heath, *Nature* **2007**, *445*, 414–417.
- [119] M. C. Jimenez-Molero, C. Dietrich-Buchecker, J.-P. Sauvage, *Chem. Commun.* **2003**, *3*, 1613.
- [120] Y. Liu, A. H. Flood, P. A. Bonvallet, S. A. Vignon, B. H. Northrop, H. R. Tseng, J. O. Jeppesen, T. J. Huang, B. Brough, M. Baller, S. Magonov, S. D. Solares, W. A. Goddard, C. M. Ho, J. Fraser Stoddart, *J. Am. Chem. Soc.* **2005**, *127*, 9745–9759.
- [121] H. Li, A. C. Fahrenbach, A. Coskun, Z. Zhu, G. Barin, Y. L. Zhao, Y. Y. Botros, J. P. Sauvage, J. F. Stoddart, *Angew. Chem. Int. Ed.* **2011**, *50*, 6782–6788.
- [122] B. Zhang, L. Sun, *Chem. Soc. Rev.* **2019**, *48*, 2216–2264.
- [123] N. Xin, J. Guan, C. Zhou, X. Chen, C. Gu, Y. Li, M. A. Ratner, A. Nitzan, J. F. Stoddart, X. Guo, *Nat. Rev. Phys.* **2019**, *1*, 211–230.
- [124] E. Katz, O. Lioubashevsky, I. Willner, *J. Am. Chem. Soc.* **2004**, *126*, 15520–15532.
- [125] L. Sheeney-Haj-Ichia, I. Willner, *J. Phys. Chem. B* **2002**, *106*, 13094–13097.
- [126] E. Katz, L. Sheeney-Haj-Ichia, I. Willner, *Angew. Chemie Int. Ed.* **2004**, *43*, 3292–3300.